Luminous *WISE*-selected Obscured, Unobscured, and Red Quasars in Stripe 82[*]

E. Glikman[1,2] , M. Lacy[3] , S. LaMassa[4] , D. Stern[5] , S. G. Djorgovski[6] , M. J. Graham[6] , T. Urrutia[7] , Larson Lovdal[1],
M. Crnogorcevic[1], H. Daniels-Koch[13], Carol B. Hundal[8], M. Urry[9,10] , E. L. Gates[11], and S. Murray[12]

[1] Department of Physics, Middlebury College, Middlebury, VT 05753, USA
[2] Visiting astronomer, Institute for Astronomy, University of Hawaii, Honolulu, HI 96822, USA
[3] National Radio Astronomy Observatory, Charlottesville, VA 22903, USA
[4] Space Telescope Science Institute, 3700 San Martin Drive, Baltimore, MD, 21218, USA
[5] Jet Propulsion Laboratory, California Institute of Technology, Pasadena, CA 91109, USA
[6] California Institute of Technology, Pasadena, CA 91125, USA
[7] Leibniz Institut für Astrophysik, An der Sternwarte 16, D-14482 Potsdam, Germany
[8] Whitin Observatory, Department of Astronomy, Wellesley College, Wellesley, MA 02481, USA
[9] Yale Center for Astronomy & Astrophysics, Physics Department, P.O. Box 208120, New Haven, CT 06520, USA
[10] Department of Physics, Yale University, P.O. Box 208121, New Haven, CT 06520, USA
[11] UCO/Lick Observatory, P.O. Box 85, Mount Hamilton, CA 95140, USA

Abstract

We present a spectroscopically complete sample of 147 infrared-color-selected active galactic nuclei (AGNs) down to a 22 μm flux limit of 20 mJy over the $\sim$270 deg^2 of the Sloan Digital Sky Survey Stripe 82 region. Most of these sources are in the QSO luminosity regime ($L_{bol} \gtrsim 10^{12} L_{\odot}$) and are found out to $z \simeq 3$. We classify the AGNs into three types, finding 57 blue, unobscured Type-1 (broad-lined) sources; 69 obscured, Type-2 (narrow-lined) sources; and 21 moderately reddened Type-1 sources (broad-lined and $E(B-V) > 0.25$). We study a subset of this sample in X-rays and analyze their obscuration to find that our spectroscopic classifications are in broad agreement with low, moderate, and large amounts of absorption for Type-1, red Type-1, and Type-2 AGNs, respectively. We also investigate how their X-ray luminosities correlate with other known bolometric luminosity indicators such as [O III] line luminosity ($L_{\rm [O~III]}$) and infrared luminosity ($L_{6\mu m}$). While the X-ray correlation with $L_{\rm [O~III]}$ is consistent with previous findings, the most infrared-luminous sources appear to deviate from established relations such that they are either underluminous in X-rays or overluminous in the infrared. Finally, we examine the luminosity function evolution of our sample, and by AGN type, in combination with the complementary, infrared-selected, AGN sample of Lacy et al. (2013), spanning over two orders of magnitude in luminosity. We find that the two obscured populations evolve differently, with reddened Type-1 AGNs dominating the obscured AGN fraction ($\sim$30%) for $L_{5\mu m} > 10^{45}$ erg s^{-1}, while the fraction of Type-2 AGNs with $L_{5\mu m} < 10^{45}$ erg s^{-1} rises sharply from 40% to 80% of the overall AGN population.

Key words: galaxies: active – galaxies: Seyfert – infrared: galaxies – quasars: general – surveys

Supporting material: machine-readable tables

1. Introduction

Arriving at a complete census of active galactic nuclei (AGNs) is necessary in order to understand the cosmic history of black hole growth and its impact on galaxy evolution. Broadly speaking, the optical spectra of AGN can be divided into three categories. "Type-1" sources are characterized by broad emission lines atop a blue continuum. "Type-2" AGNs have only narrow emission lines atop a diminished continuum that may also show stellar absorption features from the host galaxy. These differences are thought to arise from the observer's different lines of sight to an axisymmetric geometry that includes an accretion disk around a black hole, surrounded by an equatorial concentration of dusty clouds (e.g., Urry & Padovani 1995; Elitzur 2012).

In addition to the orientation-based variation in the multi-wavelength properties of AGNs, there is another class of reddened Type-1 sources that shows an AGN-dominated continuum with broad emission lines—implying a more face-on viewing angle toward the accretion disk. Such sources are well fit by a Type-1 spectrum that is moderately dust reddened. These so-called "red quasars" have red optical colors that are easily confused with low-mass stars, making them exceedingly difficult to identify with optical color selection alone (Richards et al. 2003; Urrutia et al. 2009). Early in the development of this field of study, small samples of red quasars were identified via radio and near-infrared selection (Webster et al. 1995; Cutri et al. 2001; Gregg et al. 2002; White et al. 2003). Subsequently, one of the largest samples of red quasars was constructed using radio sources in the Faint Images of the Radio Sky at Twenty cm (FIRST; Becker et al. 1995) survey combined with near-infrared Two Micron All-Sky Survey (2MASS; Skrutskie et al. 2006) detections. This sample contains $\gtrsim$120 sources with $E(B-V) > 0.1$ spanning a redshift range of $0.1 \lesssim z \lesssim 3$ (F2M; Glikman et al. 2004, 2007, 2012; Urrutia et al. 2009). The F2M selection required a radio detection to improve efficiency and avoid contamination from Galactic stars but limited the study to $\sim$10% of all quasars that are detected in large radio surveys (Becker et al. 2000; Ivezić et al. 2002).

Mid-IR AGN selection offers an opportunity to avoid stars without requiring a radio detection and has enabled the

[12] Deceased.
[13] Bowdoin College.

construction of more complete samples of luminous quasars in the mid-IR (Lacy et al. 2004; Stern et al. 2005; Donley et al. 2012; Mateos et al. 2012; Stern et al. 2012; Assef et al. 2013). These samples enable investigations into the evolution and the luminosity dependence of dusty and Type-2 AGN fractions. Lacy et al. (2013) presented a sample of 527 mid-IR-selected AGNs in a tiered survey of various *Spitzer* fields with a range of areas and depths. Lacy et al. (2015) compared the demographics of the three classes of AGNs and found that obscured quasars evolve differently from unobscured quasars. However, a key limitation of these studies has been the small coverage area of the cryogenic *Spitzer*[14] surveys (total ~65 deg²), which means that rare, high-luminosity objects are missing from these samples. This makes it difficult to decouple the redshift- and luminosity-dependent effects to gain a more complete understanding of AGN evolution. To span the luminosity–redshift space and identify large, statistically meaningful samples of such objects requires wide-field infrared photometry.

The *Wide-Field Infrared Survey Explorer* (*WISE*) conducted an all-sky survey at mid-IR wavelengths. The All-Sky Data Release in 2012 provided 3.4, 4.6, 12, and 22 μm measurements down to flux densities of 0.08, 0.11, 1, and 6 mJy, respectively (5σ point-source sensitivities; Wright et al. 2010). This depth and area coverage offer an opportunity to extend the results of Lacy et al. (2015) to the most luminous AGNs at low redshifts.

WISE has proven to be very successful at disentangling quasars from stars and galaxies, because they lie in a distinct region in color–color space (see Figure 12 of Wright et al. 2010). These colors are a result of quasars' continuously rising spectral energy distribution (SED) without any strong breaks in this wavelength region, regardless of the presence of dust. And since mid-IR wavelengths are far less affected by dust than optical and near-IR wavelengths, *WISE* selection can find Type-2 and red quasars that have been missed by optical quasar surveys.

In this paper, we present a study in which we use *WISE* mid-IR color selection to construct a complete sample of quasars over the Sloan Digital Sky Survey (SDSS) Stripe 82 region, whose area is wide enough to begin identifying the rare luminous sources we are after. Throughout this work, we adopt the concordance ΛCDM cosmology with $H_0 = 70$ km s^{-1} Mpc^{-1}, $\Omega_M = 0.3$, and $\Omega_\Lambda = 0.7$ when computing cosmology-dependent values (Bennett et al. 2013).

2. Sample Selection

SDSS (York et al. 2000) covered more than a quarter of the sky with five-band optical imaging. The survey also includes targeted spectroscopy of over 1.6 million sources during its first seven data releases. Most of the survey's coverage is in the north Galactic cap. However, one survey stripe that straddles the celestial equator in the south Galactic cap ("Stripe 82") was repeatedly scanned by SDSS ~70–90 times, reaching ~2 mag deeper than a single-epoch SDSS scan (Jiang et al. 2014). Stripe 82 covers an equatorial region spanning a range in right ascension of $\alpha = -50°$ to $+ 59°$ and in declination of $\delta = -1°\!.25$ to $1°\!.25$ for a total area of 272.5 deg² that is accessible for follow-up studies to both northern and southern telescopes. The region also contains a
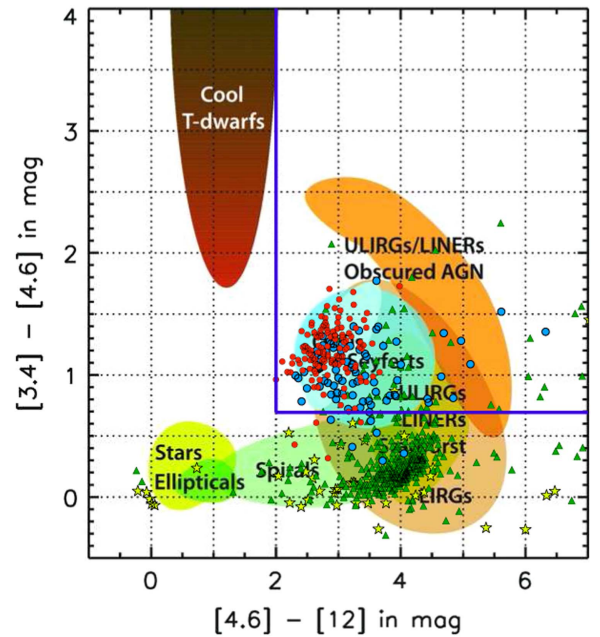
Figure 1. We reproduce Figure 12 from Wright et al. (2010) showing the location of various astrophysical objects in *WISE* color–color space. We plot objects with SDSS identifications of QSO (blue circles), GALAXY (green triangles), and STAR (yellow stars). The red circles are the F2M red quasars identified by Glikman et al. (2012). Based on the location of quasars in this space, we define color cuts to maximize our efficiency, shown with thick blue lines.

wealth of multiwavelength observations from X-rays (LaMassa et al. 2013a, 2013b, 2016c) through infrared (SpIES, SHELA; Papovich et al. 2016; Timlin et al. 2016) and radio (Hodge et al. 2011). While these multiwavelength data do not cover the entire Stripe 82 region, we search the full Stripe 82 area in this study.

### 2.1. WISE Infrared Color Selection

We began by selecting all sources with a flux density brighter than 20 mJy in the 22 μm (*W4*) band (corresponding to a cut of 6.55 mag on the Vega photometric system) from the "AllWISE" catalog overlapping the Stripe 82 borders (10,837 sources). We then match these sources to the SDSS DR9 spectroscopic database (Ahn et al. 2012) to explore the *WISE* colors of known quasars.

Figure 1 shows the location of these spectroscopically identified sources in the *WISE* color–color space as depicted in Wright et al. (2010).[15] Blue circles are SDSS-classified quasars that overlap the Stripe 82 region, green triangles are galaxies, and yellow stars are Galactic stars (Bolton et al. 2012; see Section 4), all with $S_{22\,\mu m} > 20$ mJy. We also plot reddened quasars from Glikman et al. (2012; red circles), which are seen to have the same *WISE* colors as the unobscured quasars. Based on these findings, and aiming to maximize quasar selection while avoiding inactive galaxies and stars, we applied the following *WISE* color cuts (shown with blue lines in Figure 1):

$$W1 - W2 > 0.7 \tag{1}$$

---

[14] Prior to the warm mission, when $\gtrsim 5\mu$m detectors were operational.

[15] Here the notations [3.4], [4.6], and [12] refer to the effective wavelengths of the *WISE* filters *W1*, *W2*, and *W3*, respectively. The corresponding nomenclature for the *WISE* filter *W4* is [22].
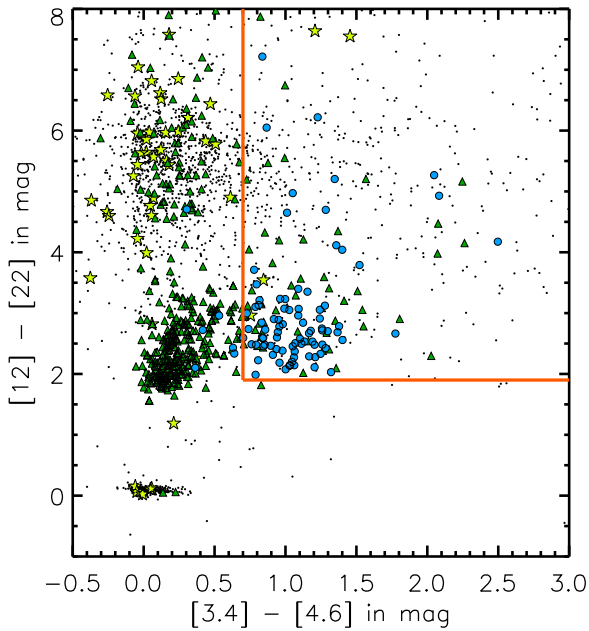
Figure 2. Colors of objects in the reddest two *WISE* bands as a function of color in the two bluest *WISE* bands. Black points are all *WISE* sources obeying our 20 mJy flux limit that lack a spectrum in SDSS. The colors and shapes are the same as in Figure 1. Our color selection, including a color cut of [12]–[22] > 1.9, is shown by an orange line. This cut further concentrates the sample to overlap where most SDSS QSOs exist with minimal contamination from galaxies.

and

$$W2 - W3 > 2. \qquad (2)$$

In addition, we examine the colors of quasars in the two longest mid-infrared bands. Figure 2 shows the location of SDSS-identified sources in $W3 - W4$ versus $W1 - W2$, along with the colors of sources without spectra. Most of the quasars have

$$W3 - W4 > 1.9, \qquad (3)$$

which we add as a third color cut to further avoid stars and other contaminants.

These cuts are similar to, though somewhat more liberal than, those used in previous works that define a "wedge" in color space, meant to track the range of infrared colors with AGN spectral index, redshift, and luminosity (Lacy et al. 2004; Stern et al. 2005; Donley et al. 2012; Mateos et al. 2012), as well as simple cuts that yield similarly effective selection (Stern et al. 2012; Assef et al. 2013). Stern et al. (2012) applied a $W1 - W2 \geqslant 0.8$ color cut to select AGNs in the COSMOS field, achieving a reliability of 95% and completeness of 78%. According to Figure 6 of Stern et al. (2012), our bluer cut in $W1 - W2$ increases the completeness by ∼10% and decreases our reliability by ∼10%, as more inactive galaxies enter the color space.[16] However, because our survey has 100% spectroscopic completeness (Section 3), we are able to trade AGN purity among our candidates in favor of recovering more AGNs.

Although AGNs emit at all wavelengths, their SEDs can be affected by obscuration, as well as by added light from star

---

[16] The different sensitivity cuts at different bandpasses between the Stern et al. (2012) study and this work—$W2 \sim 15$ versus $W4 = 6.55$, respectively—limit a direct comparison between the two studies.

formation. Therefore, in general, no single wavelength regime can be used to find all AGNs. Significant work has been done to explore biases and incompletenesses of AGN surveys selected at different wavelengths and flux limits (e.g., Eckart et al. 2010; Juneau et al. 2013; Mendez et al. 2013; Messias et al. 2014), arriving at a general consensus that infrared selection is most effective at identifying the most intrinsically luminous AGNs, which is the regime targeted in this work. We address the role of wide-field X-ray selection in Section 5.2.

The *WISE* catalog assigns each source a "contamination and confusion" flag (cc_flags), which indicates the fidelity of the quoted photometry in the catalog in the form of a four-character string corresponding to each of the four photometric bands. Because our flux limit is imposed in the 22μm band, we keep only sources with the highest photometric quality flags in that band, restricting our sample to sources with cc_flags = ''***0'' (where * indicates allowing all flags in the other bands).

We noticed an excess of sources around $\alpha = 00^h08^m37^s$, $\delta = -00°25'20''$, where ∼90% of the objects were clustered (radius ∼ 15'). The *WISE* image of the region reveals a bright extended feature with clear diffraction spikes that were not flagged as suspect. We chose to conservatively excise the right ascension range $00^h < \alpha < 00^h15^m$ from Stripe 82 to eliminate the entire contaminated region.

Applying the infrared color criteria as outlined in Equations (1)–(3), as well as the quality cuts, reduces the sample size to 215 sources and shrinks the survey area by $9.4\,\mathrm{deg}^2$ to $263\,\mathrm{deg}^2$. Of these, 209 have a counterpart in the SDSS DR9 database within a $3''$ search radius, and of these, 168 have spectroscopic identifications in SDSS.[17] The six *WISE* sources lacking a match in SDSS appear to be artifacts in the *WISE* catalog. We inspected their *WISE* image cutouts and found no source at the cataloged position. All these sources were within $20''$ of bright, nearby galaxies ($z \lesssim 0.05$) with SDSS spectra, some of which obeyed our color cuts and were thus already part of our sample.
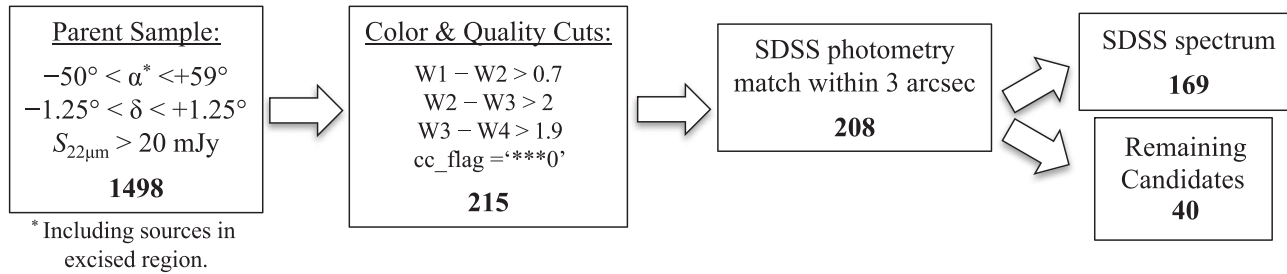
3. Spectroscopy

3.1. Archival Spectroscopy

Of the 169 objects with SDSS spectra, 107 are classified as QSO and 61 are classified as GALAXY by the SDSS classification pipeline (Bolton et al. 2012). We first examined the SDSS spectra with a QSO classification by eye and found three sources with erroneously assigned redshifts. Two of these, SDSS J012925.82−005900.2 and SDSS J005009.81−003900.3, were assigned very high redshifts, $z = 6.10$ and $z = 6.03$, respectively, by the SDSS pipeline. However, visual inspection of their spectra shows that the lines identified as Lyα are actually unusually broad [O III] λ5007, resulting in redshifts of 0.710 and 0.728, respectively. At these corrected redshifts we also identify [O II] λ3727 and Hβ, among other lines. These sources also show reddened continua; our reddening fits (Section 5.1) find that they have $E(B-V)$ of 0.49 and 0.27 mag, respectively. Another source, SDSS J005621.72+003235.7, was assigned the redshift $z = 0.132$ by

---

[17] All but two of these 169 sources had a spectrum in SDSS DR9. The remaining sources had a spectrum in SDSS DR14. One object, SDSS J023301.24+002515.03, though well detected in SDSS imaging, lacks a photometric entry in the SDSS catalog but has a spectrum that we obtained and included in our analysis. This is a known Seyfert 2 galaxy (UGC 2024; Schmitt et al. 2003).

Parent Sample:	Color & Quality Cuts:	SDSS photometry match within 3 arcsec	SDSS spectrum
$-50° < \alpha^* < +59°$ $-1.25° < \delta < +1.25°$ $S_{22\mu m} > 20$ mJy **1498**	$W1 - W2 > 0.7$ $W2 - W3 > 2$ $W3 - W4 > 1.9$ cc_flag ='***0' **215**	**208**	**169** Remaining Candidates **40**

* Including sources in excised region.

Figure 3. Flowchart showing the process for selecting the AGN sample in this work. Each box reports the final candidate selection, with the number of sources that passed each stage shown in boldface.

erroneously identifying [O III] $\lambda5007$ as Hα. The corrected redshift of this source is $z = 0.484$. This leaves 40 *WISE*-selected sources lacking spectroscopic identification in SDSS.

We searched the literature, through the NASA Extragalactic Database (NED), to check whether any of these sources had previously known redshifts, and we identify 10 such sources. Five of these are ULIRGs with $z = 0.1$–0.3 (Strauss et al. 1992; Stanford et al. 2000), and two are nearby Seyfert galaxies at $z = 0.031$ (Boroson & Meyers 1992) and $z = 0.040$ (Huchra et al. 1999). Another source is described as a "Wolf-Rayet galaxy" at $z = 0.058$ by Schaerer et al. (1999) and appears in NED under the name UM 420. Finally, we detect star-forming galaxy UGC 12348, at $z = 0.0254$ (Huchra et al. 1999).

Consistent with the design of our color selection, which was intended to find red quasars, we recover the one F2M red quasar (Glikman et al. 2012) overlapping our survey area that lacks a spectrum in SDSS. Two other F2M red quasars (F2M0156−0058 and F2M0036−0113) have spectra in SDSS and are also recovered by our selection method; a final F2M red quasar (F2M0136−0052) misses our W4 flux limit, with $S_{22\,\mu m} = 11.3$ mJy.

We also recover an extremely infrared-luminous quasar, W2305−0039, at $z = 3.106$ identified among a sample of hot dust-obscured galaxies (Hot DOGs; Tsai et al. 2015). This extreme quasar is also the optically faintest source in our sample. Hot DOGs have many properties in common with dust-reddened quasars (see Wu et al. 2012; Fan et al. 2016), and the spectrum of W2305−0039 shows moderately broad Lyα emission (FWHM ~ 1800 km s^{-1}) and weak, but possibly broader, C IV (P. Eisenhardt 2018, personal communication). We consider this object as a red Type-1 AGN in our subsequent analysis.

Figure 3 shows a flowchart of our selection process. Table 1 lists the identification of the 40 remaining candidates, as well as their positions, magnitudes, and spectroscopic information, including source classification and redshift. We identify the sources in this table with the prefix "Ws82," which is an abbreviation of "*WISE* Stripe 82." Some sources have detections in 2MASS, and we label them with the prefix "W2M," which is an abbreviation of "*WISE* 2MASS," as this subset population will be expanded in a future study. For objects lacking a detection in 2MASS, we report their near-infrared magnitudes from the UKIRT Infrared Deep Sky Survey (UKIDSS; Lawrence et al. 2007), which reaches ~ 2.5 mag deeper than 2MASS in the K band. When finding a counterpart in either near-infrared survey, we use the closest match within a $2''$ search radius to the *WISE* coordinate.

3.2. Spectroscopic Observations

We obtained optical and/or near-infrared spectra for all 29 candidates that lack any spectroscopic identification ($29 = 40 - 11$ from the literature), as well as for five sources with redshifts in the literature. Together with the SDSS and NED classifications, we have spectroscopy in hand or know the redshifts of all the sources that obey our selection criteria.

3.2.1. Near-infrared Spectroscopy

We performed near-infrared spectroscopy at the NASA Infrared Telescope Facility (IRTF) on UT 2012 September 21–22 and UT 2016 August 17 with the SpeX spectrograph (Rayner et al. 2003). We obtained spectra for 12 sources lacking a redshift in the literature. The observing conditions were excellent (mostly clear, and $0''5$–$0''8$ seeing). We used either the $0''5$ or $0''8$ slit, as appropriate, and integrated for between 40 and 56 minutes per target, depending on the brightness of the source. We obtained a spectrum of telluric standard stars of type A0V at similar airmass to our targets immediately after each observation.

On UT 2015 October 8 and November 4 we also obtained near-infrared spectra of seven QSOs whose optical spectra from SDSS were well fit by a reddened QSO template with $E(B - V) > 0.25$ (Section 5.1). We used the TripleSpec cross-dispersed spectrograph (Wilson et al. 2004) on the Apache Point Observatory 3.5 m telescope. And, on UT 2017 November 1 we obtained four near-infrared spectra of such reddened QSOs with the TripleSpec instrument on the Hale $200''$ Telescope at Palomar Observatory.

All near-infrared spectra were reduced using the Spextool software package (Cushing et al. 2004), which was designed to reduce SpeX data from IRTF. A modified version of the software was used for the TripleSpec data from both the Palomar and APO observatories. We corrected the spectra for telluric absorption following Vacca et al. (2003).

3.2.2. Optical Spectroscopy

Optical spectra for 18 candidates were obtained with the 3 m Shane telescope at the Lick observatory using the dual-arm Kast Spectrograph on UT 2012 October 19–21 with integration times ranging from 20 minutes to 1 hr per target. A $2''$ slit was used, aligned with the parallactic angle. The 5500 Å dichroic was used to split the light between the red and blue arms. In the red arm, a 600 line mm^{-1} grating blazed to 7500 Å was used, and in the blue arm a 600 line mm^{-1} grism blazed to 4310 Å was used.

One source, W2M J2216+0058, originally studied by Stanford et al. (2000), was observed with the Double

Table 1
WISE-selected AGN Candidates in Stripe 82 Lacking SDSS Spectroscopy

Name	g^{a} (mag)	r^{a} (mag)	i^{a} (mag)	J^{b} (mag)	K^{b} (mag)	$W1^{b}$ (mag)	$W2^{b}$ (mag)	$W3^{b}$ (mag)	$W4^{b}$ (mag)	Redshift	Class	Spectrum	References
Ws82 J002119.92+003804.0	20.08	18.94	18.66	17.88	⋯	14.22	13.08	9.15	6.33	0.234	QSO-2	Kast	
W2M J003009.08−002744.2	20.35	19.18	18.44	16.50	14.20	13.86	12.81	8.90	6.48	0.242	QSO-2	LRIS	S00
Ws82 J003514.49+011430.4	21.50	20.85	20.30	⋯	16.94	14.86	13.44	9.39	6.53	0.805	redQSO	Kast/TSpec	
W2M J010335.35−005527.2	19.17	17.92	18.28	16.50	15.00	13.24	11.59	7.78	4.84	0.268	QSO-2	Kast/SpeX	
Ws82 J015005.29−010854.0	20.90	20.21	19.74	18.73	⋯	14.19	12.57	9.21	6.48	0.519	GALAXY	Kast	
Ws82 J021358.58−005745.3	20.10	18.90	18.74	17.69	15.85	13.90	12.48	9.11	6.50	0.261	QSO-2	LRIS	
Ws82 J022054.52 + 003324.3	15.76	15.84	15.21	17.77	15.94	12.93	11.41	7.58	4.26	0.058	GALAXY	LRIS	S99
Ws82 J022814.05−005457.4	21.51	20.99	20.14	18.87	16.46	13.89	12.29	9.00	6.39	0.629	QSO-2	Kast	
W2M J025353.92−004615.3	19.60	18.88	18.28	16.78	15.02	14.46	13.50	8.94	6.54	0.182	QSO-2	LRIS	
Ws82 J025824.21−001038.3	22.35	21.45	20.88	18.86	16.70	13.89	11.92	7.82	5.48	0.969	redQSO	LRIS	
W2M J030654.88+010833.6	19.39	18.05	17.53	16.36	14.49	13.22	12.02	9.19	6.30	0.189	QSO-2	Kast/SpeX	
W2M J030725.00−001901.0	19.23	18.35	18.05	16.83	13.53	11.43	10.26	7.38	4.88	0.269	QSO-2	LRIS	S00
W2M J033810.37+011418.2	16.30	15.89	15.43	14.50	13.34	12.23	10.81	6.67	3.48	0.040	QSO-2	⋯	H99
W2M J034740.19+010513.9	14.79	14.46	14.34	12.99	10.89	9.23	8.26	5.33	3.03	0.031	QSO	⋯	B92
W2M J034902.65+005430.5	18.97	17.92	17.14	15.84	13.35	11.59	10.23	7.31	4.86	0.109	QSO-2	Kast/SpeX	
W2M J035442.21+003703.2	20.05	18.83	17.92	15.68	14.37	13.72	13.01	8.51	5.08	0.152	QSO-2	⋯	S92
Ws82 J205207.64−010851.5	20.35	19.51	19.23	18.11	16.10	14.56	13.43	9.63	6.55	0.289	QSO-2	Kast	
Ws82 J205449.61+004152.9	20.47	19.15	18.47	17.84	15.62	13.33	11.67	8.46	5.45	0.203	QSO-2	LRIS	
W2M J205740.76+005418.6	19.75	18.36	18.09	17.11	15.09	13.19	11.79	8.73	6.23	0.332	QSO-2	Kast/SpeX	
Ws82 J211025.70−010157.3	19.41	18.44	18.03	17.46	15.82	13.94	12.65	9.19	6.52	0.122	QSO-2	Kast	
W2M J211824.24+002311.6	19.60	18.26	17.65	16.96	14.55	12.87	11.55	8.68	6.30	0.22	GALAXY	LRIS/SpeX	
Ws82 J213634.25−011208.0	20.26	19.51	18.97	18.04	16.17	14.00	12.55	8.20	5.49	0.631	GALAXY	LRIS	S00
Ws82 J213853.11+001946.1	22.33	20.85	20.03	18.54	15.55	13.40	12.01	8.87	6.54	0.518	GALAXY	Kast	
Ws82 J214825.35−001132.2	21.34	20.30	19.61	18.50	15.49	13.39	12.00	8.81	6.38	0.64	QSO-2	Kast	
W2M J215214.98−005151.8	18.78	18.53	18.14	16.83	15.05	13.43	12.25	9.19	6.33	0.582	redQSO	Kast/SpeX	
Ws82 J220128.06−003812.0	21.26	20.25	19.54	18.01	15.93	14.21	12.82	9.04	6.30	0.498	QSO-2	Kast	
Ws82 J221220.21+003337.9	20.59	20.96	20.48	17.87	15.90	13.09	11.62	7.53	4.33	999.0	?^{c}	SpeX	
W2M J221602.69+005811.0	19.67	18.73	18.16	16.86	15.37	14.19	12.49	9.09	6.43	0.211	QSO-2	DBSP	S00
W2M J221633.72−005451.6	19.55	18.26	17.57	15.92	13.74	12.27	11.25	8.59	6.10	0.200	redQSO	⋯	G07
Ws82 J222320.22+011350.9	20.17	19.05	18.59	17.62	15.78	14.09	12.61	8.61	6.24	0.252	QSO-2	Kast	
Ws82 J224056.59+003043.7	21.40	20.34	19.84	⋯	16.00	14.41	13.00	9.31	6.06	0.278	QSO-2	Kast	
W2M J224632.74+010300.5	18.13	17.17	16.65	15.59	14.31	13.24	12.51	8.56	6.13	0.122	QSO-2	Kast/SpeX	
W2M J225224.15−003144.7	19.10	18.39	17.90	16.63	15.00	13.42	11.91	9.14	6.27	0.167	GALAXY	Kast/SpeX	
Ws82 J225523.32+004943.1	22.49	20.88	19.59	17.16	15.33	13.20	11.79	8.73	6.31	0.812	redQSO	LRIS/SpeX	
W2M J230518.83+001122.2	14.54	13.67	13.24	13.52	11.53	10.04	9.20	6.31	3.72	0.025	GALAXY	⋯	H99
Ws82 J230525.88−003925.7	25.87	23.16	22.40	⋯	...	17.00	16.02	9.91	6.33	3.106	redQSO	⋯	T15
Ws82 J233056.19−001234.9	22.17	21.37	20.85	19.25	16.87	13.68	11.57	8.18	6.23	0.463	QSO-2	LRIS	
Ws82 J234302.80−005934.2	21.55	20.79	20.14	18.67	16.26	13.75	12.14	8.68	5.97	0.767	QSO-2	LRIS	
Ws82 J234658.41−003806.5	24.10	21.88	20.83	18.39	15.36	13.09	11.42	8.31	6.35	0.810	redQSO	LRIS/SpeX	
W2M J235535.83−011444.2	19.47	18.44	18.10	16.76	14.92	12.99	11.79	8.70	6.32	0.323	QSO-2	LRIS/SpeX	

Notes.
[a] AB magnitudes.
[b] Vega magnitudes.
[c] This source shows no AGN signatures. See the Appendix for details.
References. B92—Boroson & Green (1992); G07—Glikman et al. (2007); H99—Huchra et al. (1999); S00—Stanford et al. (2000); S92—Strauss et al. (1992); S99—Schaerer et al. (1999); T15—Tsai et al. (2015).

(This table is available in machine-readable form.)

Spectrograph on the Hale 200″ Telescope at Palomar Observatory on UT 2017 September 14. Two 600 s exposures were used with a 1″ slit under relatively poor seeing and foggy conditions.

We obtained optical spectra of 14 sources with the Low Resolution Imaging Spectrograph (LRIS; Oke et al. 1995) at the Keck I telescope. Three sources were observed on UT 2015 May 24 (Ws82 J2054+0041, W2M J2118+0023, W2M J2355 −0114), one source was observed on UT 2016 September 8 (Ws82 J0213−0057), another source was observed on UT 2016 September 29 (W2M J2255+0049), one spectrum was obtained on UT 2017 September 14[18] (Ws82 J2346−0038), six spectra were obtained on UT 2017 September 16 (W2M J0030 −0027, Ws82 J0220+0033, Ws82 J0253−0046, W2M J0307 −0019, Ws82 J2136−0112, Ws82 J2343−0059), and two final sources were observed on UT 2017 October 17 (Ws82 0258 −0010, Ws82 2330−0012). Integration times ranged between 600 and 900 s.

For all Keck observations, we used long slits with widths between 1″0 and 1″5, the 5600 Å dichroic to split the light, and the 400 line mm^{-1} grating on the red arm ($\lambda_{\mathrm{blaze}} = 8500$ Å). For the 2015 May and 2016 September observing runs, we used the 400 line mm^{-1} grism on the blue arm ($\lambda_{\mathrm{blaze}} = 3400$ Å), while the rest of the observing runs used the 600 line mm^{-1} grism on the blue arm ($\lambda_{\mathrm{blaze}} = 4000$ Å). We processed the data using standard techniques within IRAF and calibrated the spectra using standard stars from Massey & Gronwall (1990) observed on the same nights using the same instrument configurations.

Figures 4(a) and (b) present a spectral atlas of the 12 sources possessing both optical and near-infrared spectra. All these sources have securely determined redshifts. We mark the locations of typical AGN emission features with vertical dashed lines.

Figures 5(a) and (b) show the 21 sources with only optical spectra from Lick, Palomar, or Keck. In Section 4.1, we use line fitting and diagnostics to determine the nature of these sources, whether they are AGN dominated or star formation dominated. Table 1 presents the final list of *WISE*-selected AGN candidates lacking an SDSS spectrum, including their photometry, redshift, classification, and spectral origin.

4. Source Classification

The classification of SDSS spectra up through DR9 was performed by Bolton et al. (2012) using χ^2 minimization to a suite of templates for each spectrum. The template fitting yielded the overall classification of GALAXY, QSO, or STAR and provided redshift estimates. Gaussian profiles were also fit to emission lines in the spectra, providing fluxes and line widths that allowed for further subclassification. In order to have a uniform analysis of the spectra obtained by us and from SDSS, we conduct our own analysis of emission-line diagnostics for classifying the sources in the entire sample.

4.1. Line Diagnostics and AGN Classification

Visual examination of the 107 SDSS spectra identified with a class of QSO in SDSS revealed that some show only

narrow lines, which means that Type-2 sources are included among these objects. We therefore measured independent BPT line diagnostics (Baldwin et al. 1981) to determine which of these sources are AGNs and which are star formation dominated (see also Veilleux & Osterbrock 1987; Kewley et al. 2001; Kauffmann et al. 2003; Kewley et al. 2006). We inspected the spectra of all QSOs with $z \lesssim 0.4$ to identify sources with only narrow emission lines and a galaxy-dominated continuum (e.g., the presence of a 4000 Å break or a flat continuum lacking the rise toward the UV seen in Type-1 quasars); 33 spectra fit these criteria.

To study the emission-line properties of these sources, we turn to the Gas AND Absorption Line Fitting code (GAN-DALF; Sarzi et al. 2006), which fits a stellar population to the host galaxy simultaneously with Gaussian profiles fitted to specified emission lines. Figure 6 shows three representative examples of the fits produced by GANDALF. We use the line fluxes output by GANDALF to plot the objects on BPT diagrams.

Objects with $z \gtrsim 0.4$ only allow the measurement of the [O III]/Hβ ratio because Hα is redshifted beyond the optical spectral range. Five sources with $z > 0.4$ showed strong narrow emission lines but no underlying host galaxy features. For these sources, we fit Gaussian profiles to all available lines needed for constructing BPT diagrams.

Figure 7 shows the resultant BPT diagrams for the 38 narrow-line spectra (33 with $z < 0.4$ and 5 with $z > 0.4$) classified as QSOs by SDSS, plotted with orange circles. We plot arrows in the leftmost panel for the higher-redshift sources lacking a measurement on the abscissa. For comparison, we also plot the 16 objects from our own spectroscopy (see below) with blue symbols. As is clear from this figure, there are many objects classified as QSO by SDSS that fail the BPT diagnostic of Kewley et al. (2001). We consider as Type-2 AGNs sources that obey the AGN criterion in *at least one* of the diagnostic panels. The five $z > 0.4$ sources are further analyzed and classified below.
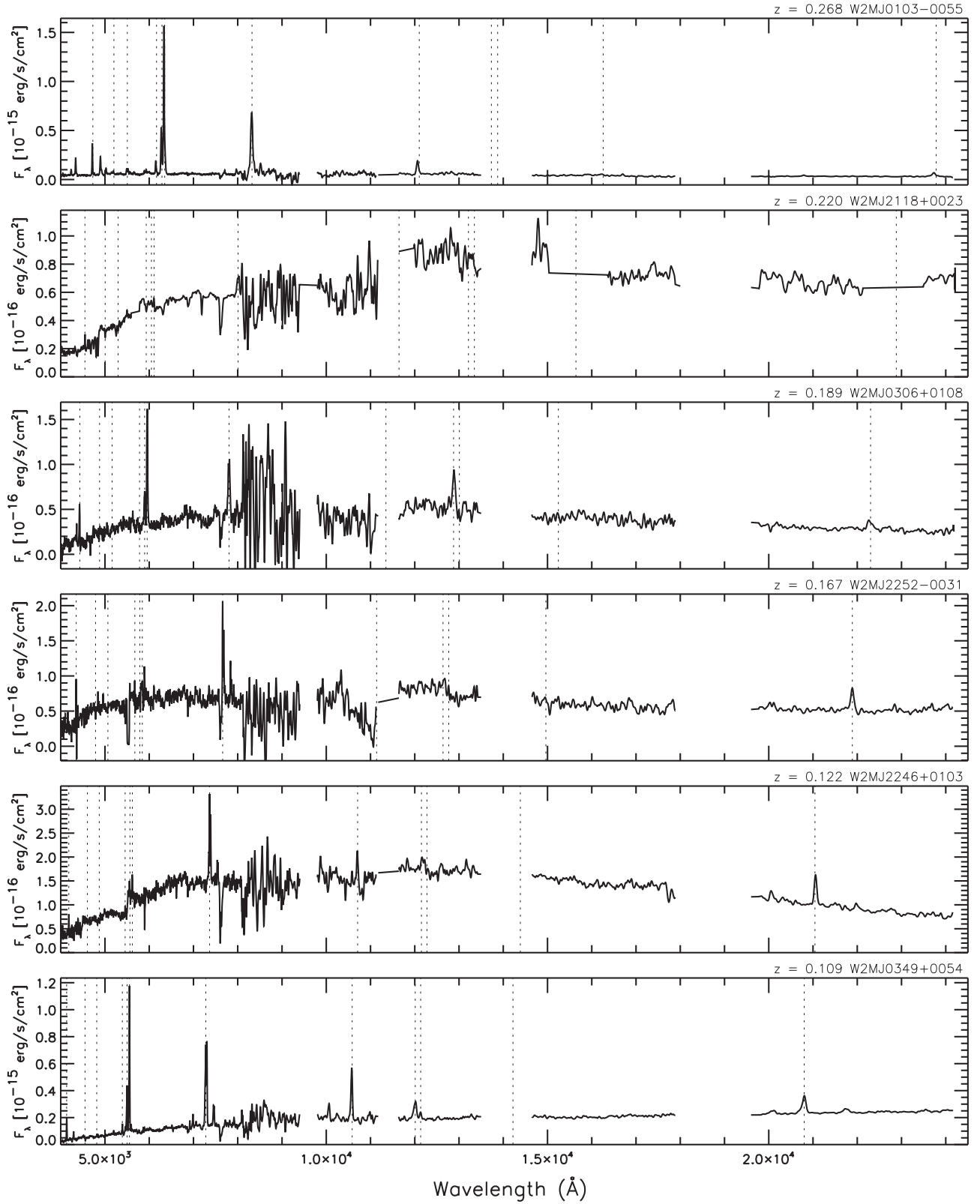
Likewise, the 62 SDSS spectra classified as *GALAXY* may have line ratios indicative of AGNs. Visual inspection of these spectra reveals that 13 have no emission-line features, and we do not consider them further. One source, SDSS J030000.57 +004827.9, revealed a broad absorption line (BAL) QSO spectrum whose deep absorption troughs may have been mistaken as a galaxy at $z = 0.568$ by the automated fitting algorithm. This source was classified by Hall et al. (2002) as an "unusual" BAL QSO at $z = 0.892$, and we add it to our Type-1 QSO tally with the corrected redshift. We repeat the process described above on the remaining spectra, using GANDALF and analyzing the resultant line ratios. This analysis resulted in 18 additional AGNs, and they are plotted in Figure 7 with green symbols.

Twenty-four of the optical spectra obtained by us (three of which were previously identified by Stanford et al. 2000) had strong line emission, and we performed BPT line diagnostics to determine which of these sources are AGNs and which are star formation dominated. We fit Gaussian profiles to H$\beta +$ [O III], [Ne III] $\lambda 3869$, [O II] $\lambda 3727$, and H$\alpha +$ [N II] and computed line ratios. While all 24 sources had available Hβ and [O III], only 13 sources had Hα and [N II]. For those 13 objects we computed [N II]/Hα and plotted them as blue circles in Figure 7. Although Hα is seen in many of our near-infrared spectra, the signal-to-noise ratio of the line was not sufficient

---

[18] This spectrum enabled a redshift determination, from the presence of [O II] and the D4000 Å break. However, bad columns on the detector chip overlapped the source spectrum, rendering the shape of the continuum unreliable.

(a)
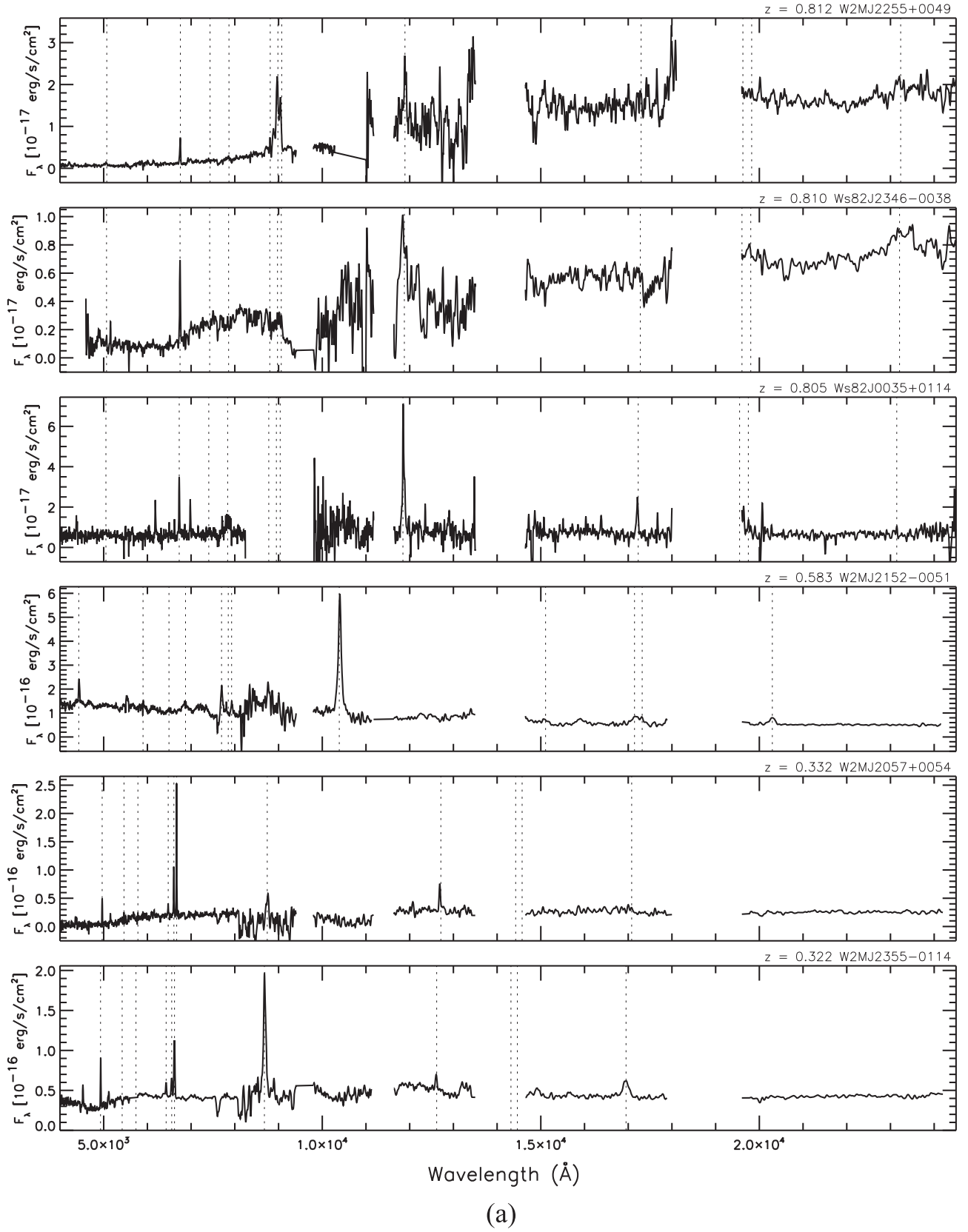
Figure 4. (a) Spectral atlas showing optical to near-infrared spectroscopy of AGN candidates for which redshifts could be determined. The spectra are sorted by decreasing redshift, with typical AGN emission lines marked by vertical dashed lines: Mg II $\lambda2798$, [O II] $\lambda3727$, Hδ $\lambda4102$, Hγ $\lambda4341$, Hβ $\lambda4861$, [O III] $\lambda\lambda4959$, 5007, Hα $\lambda6563$, He I $\lambda10830$, Paγ λ 10941, Paβ $\lambda12822$, and Paα $\lambda18756$. (b) Same as panel (a).

(b)

Figure 4. (Continued.)

for decomposition of the Hα + [N II] complex. We plot sources that did not have Hα in their optical spectrum as blue arrows to show their position along the vertical axis.

Trouille et al. (2011) devised an alternative AGN diagnostic for higher-redshift sources whose Hα + [N II] lines are shifted beyond the optical range. Their so-called

(a)
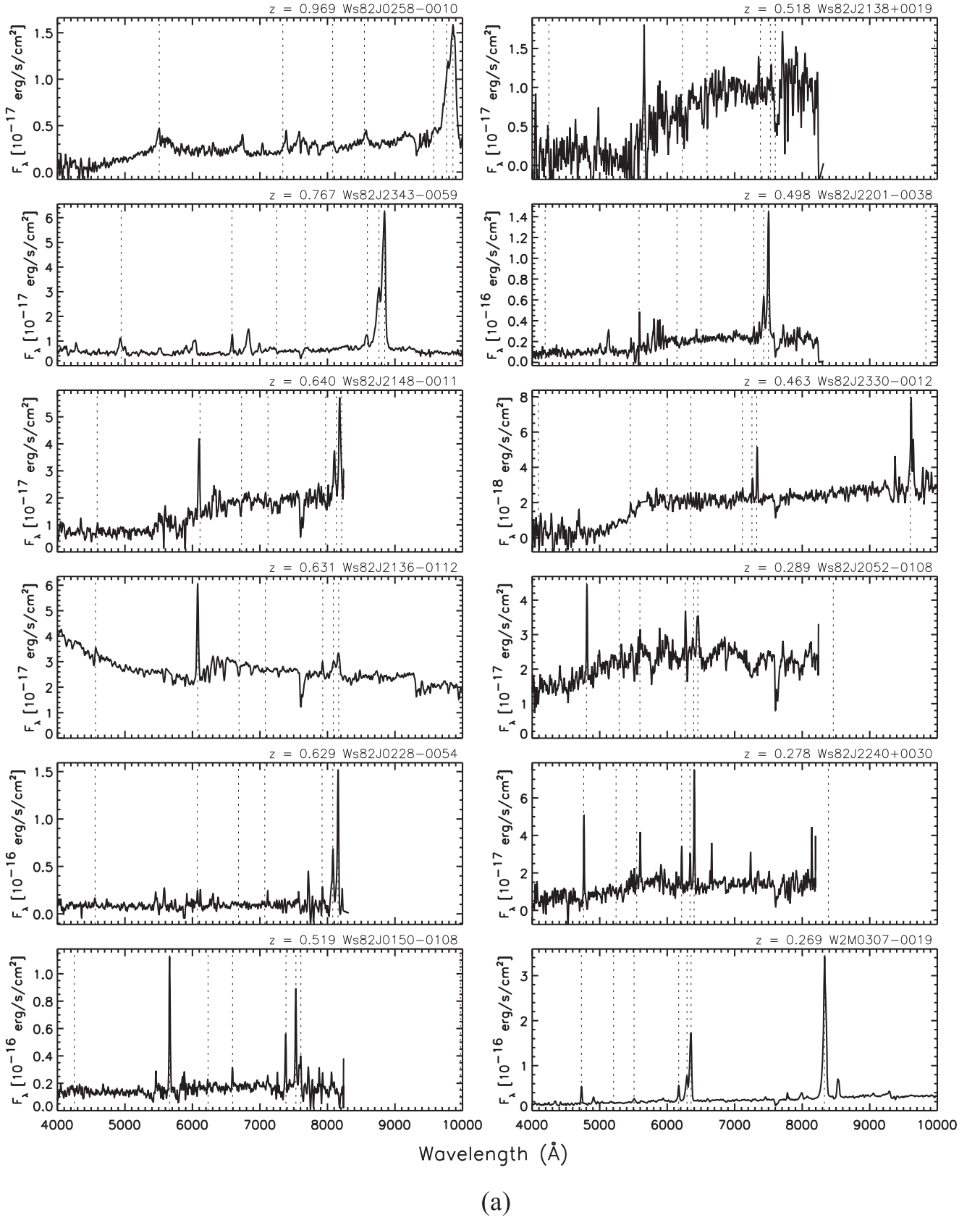
Figure 5. (a) Spectral atlas of *WISE*-selected AGN candidates with only an optical spectrum sorted by decreasing redshift. Included are two spectra with previous identifications in the literature from Stanford et al. (2000) (Ws82 J2136−0112, W2M J0307−0019). (b) Same as panel (b). Included are three spectra with previous identifications in the literature from Stanford et al. (2000) (W2M J0030−0027, W2M J2216+0058) and from Schaerer et al. (1999) (Ws82 J0220+0033).
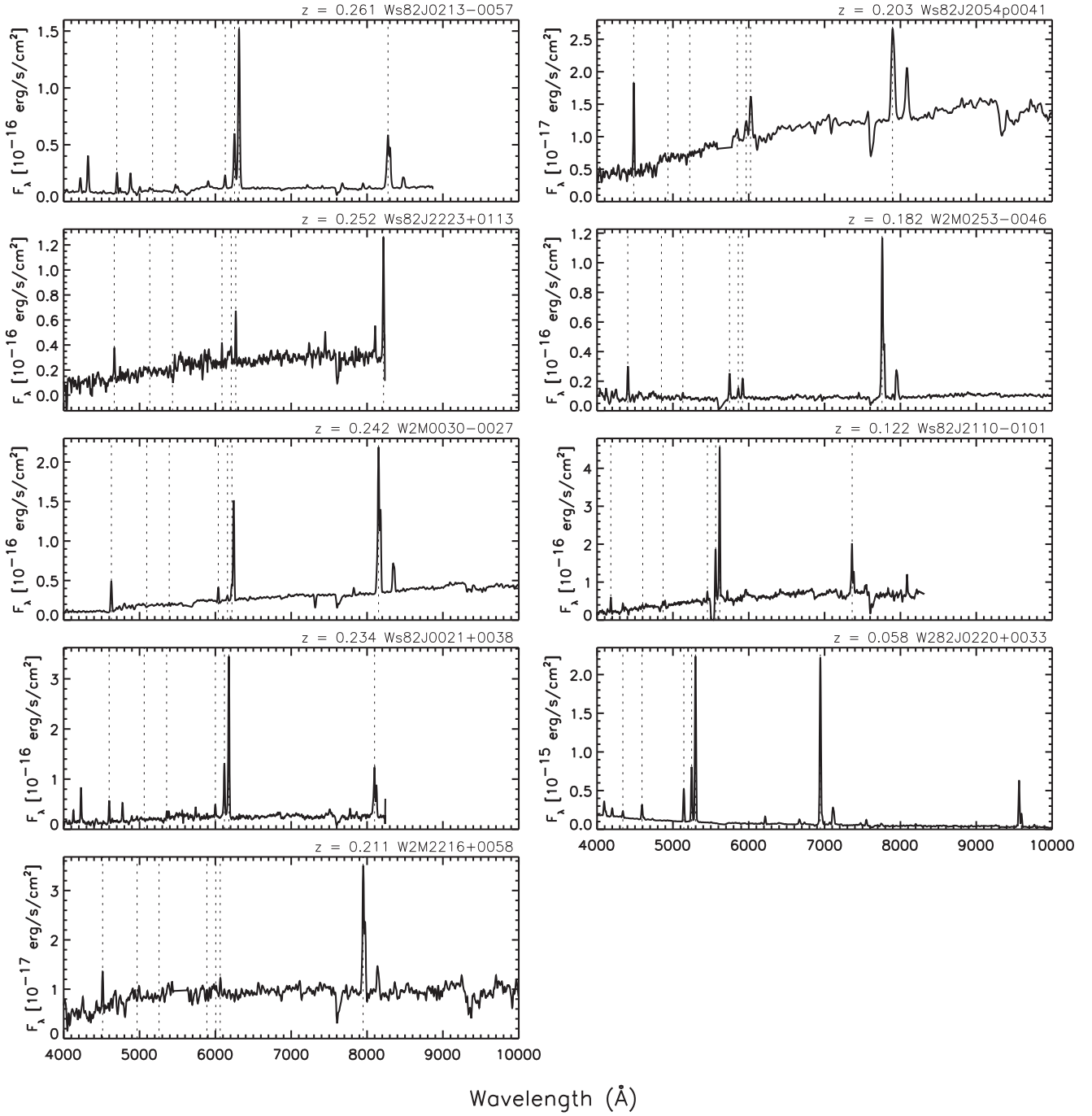
(b)

Figure 5. (Continued.)

TBT diagram, which plots rest-frame $(g - z)$[19] color versus [Ne III]/[O II] ratio, finds that AGNs lie in regions of red $^{0.0}(g - z)$ color and $\log([\text{Ne III}]/[\text{O II}]) > -1.0$. In Figure 8 we plot $^{0.0}(g - z)$ versus [Ne III]/[O II] for the 24 narrow-line sources, as well as the five higher-redshift sources with SDSS spectra (blue symbols).

To estimate rest-frame colors, we compute k-corrections for a starburst template from Kinney et al. (1996) and for a Type-2 AGN (IC 3639; Storchi-Bergmann et al. 1995) and plot their k-corrected colors with triangles and asterisks, respectively. We also plot the observed $(g - z)$ color with circles and connect the symbols for a given source with a gray line to guide the eye and give the reader a sense for the size of the k-correction. The dashed line is the starburst/AGN dividing line presented by Trouille et al. (2011).

---

[19] The rest-frame color is denoted by Trouille et al. (2011) as $^{0.0}(g - z)$. We carry forward this notation in our analysis.
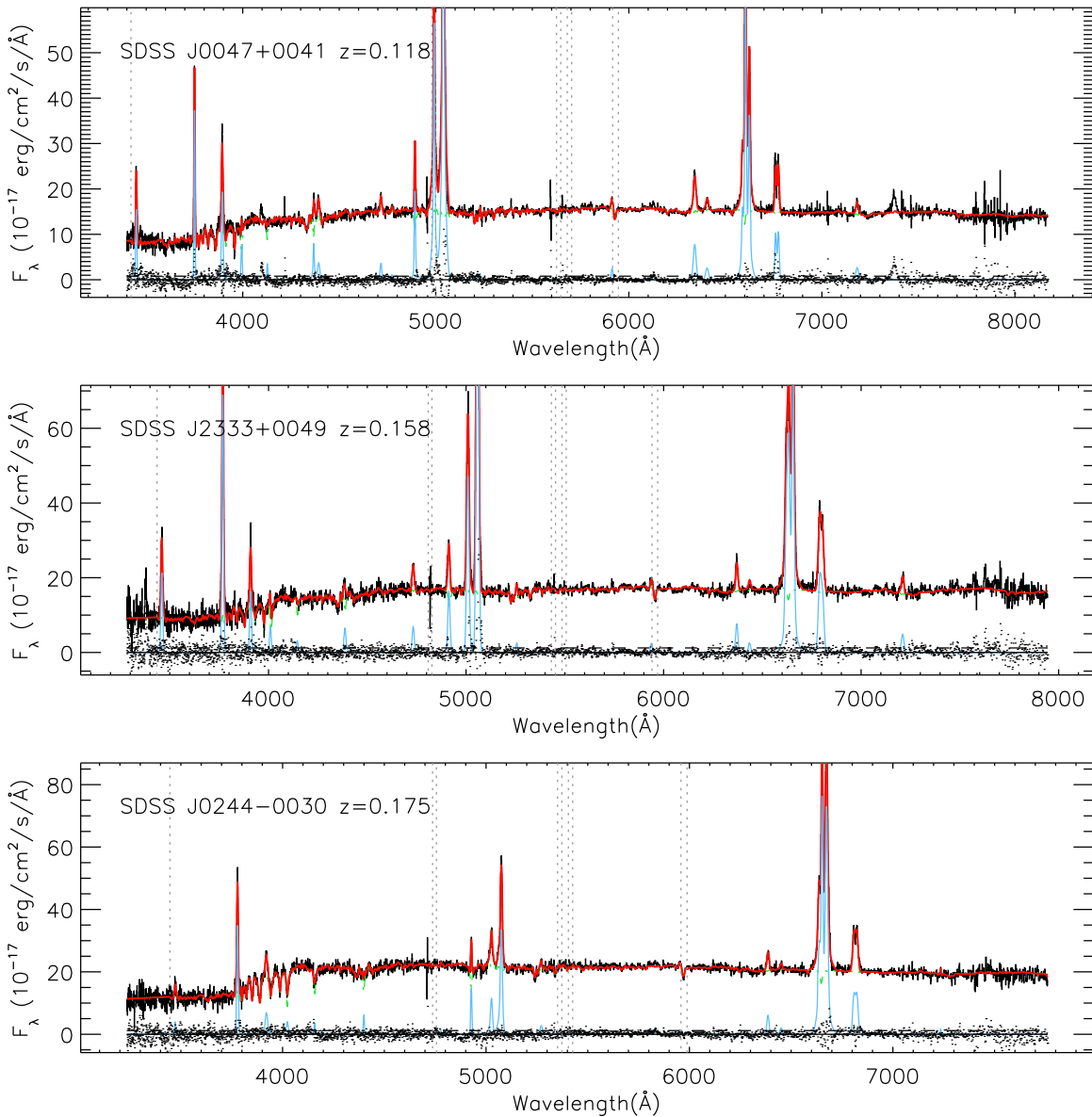
Figure 6. Three representative SDSS spectra (black line) with GANDALF fit overlaid (red line). The blue line shows the emission-line spectrum, while a green line seen beneath the red line shows the combination of Bruzual & Charlot (2003) templates that best fit the host galaxy.

One source, Ws82 J0150−0108, is found near the star-formation-dominated region of the diagram (when considering the starburst-template-based k-correction). While this source lacks Hα coverage in its optical spectrum, it had the lowest [O III]/Hβ ratio, making it likely to be in the starburst region of the BPT diagram. We classify it as a galaxy. The $^{0.0}(g - z)$ versus log([Ne III]/[O II]) values of another source, Ws82 J0220+0033, are far below the axes (−0.79, −1.70), and it has been previously classified by Schaerer et al. (1999) as a Wolf-Rayet galaxy. We do not consider this source to be an AGN.

Of the 34 sources for which we obtained spectra—remaining consistent with our criterion requiring an AGN diagnosis by at least one method—we classify 22 of the 24 narrow-line-emitting objects as Type-2 AGNs. Table 2 lists the line ratios computed for these 24 sources and the five higher-redshift sources with SDSS spectra, which we could not classify via BPT diagnostics, as shown in Figure 7.

Five objects for which we obtained spectra, Ws82 J0035+0114 ($z = 0.805$), Ws82 J0258−0010 ($z = 0.969$), W2M J2152-0051 ($z = 0.583$), W2M J2255+0049 ($z = 0.812$), and Ws82 J2346 −0038 ($z = 0.810$), have both broad and narrow emission lines and red continua, and we classify them as red Type-1 AGNs.

Table 3 lists the 115 sources with SDSS spectroscopy that showed AGN signatures by our line diagnostic methods (Section 4.1). The column listing the source classification is the result of our refined process, described above. Together with Table 1, these sources comprise our parent AGN sample.

4.2. Non-AGNs

Among the sources with SDSS spectra, 62 did not meet our criteria for being AGNs. In addition, eight sources for which we obtained spectra were classified as galaxies either through their line ratios or through the absence of lines atop a galaxy
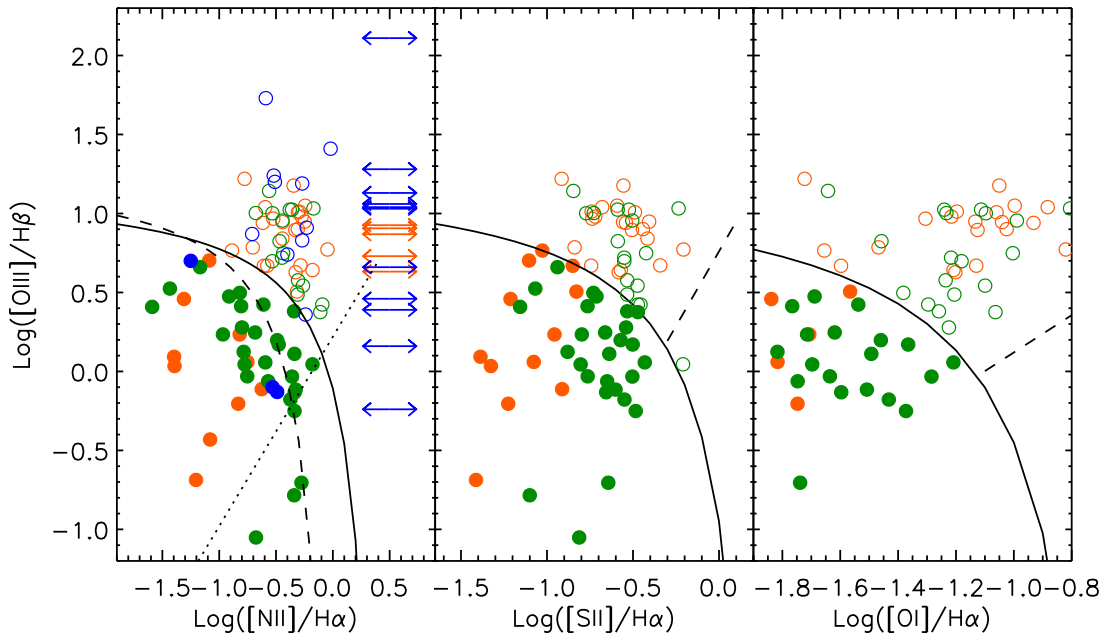
Figure 7. BPT diagrams for narrow-line-emitting sources in our sample. SDSS spectra classified as QSO, but which only show narrow emission lines, are plotted with orange symbols. SDSS spectra classified as GALAXY are plotted with green symbols. Blue symbols show the line ratios for the objects lacking SDSS spectra for which we obtained independent spectroscopic measurements. Solid lines are the boundaries separating star-formation-dominated from AGN-dominated emission from Kewley et al. (2001), while the dashed line is the composite boundary defined by Kauffmann et al. (2003). Sources that fall below the starburst boundary are shown as filled circles, while open circles are likely AGN dominated. The dotted line is the boundary used by Bolton et al. (2012) to identify AGN emission in objects with GALAXY classifications.

spectrum. One of these galaxies has an unusual morphology and complex spectroscopy, which we describe in more detail in the Appendix. As shown in Figure 9, which plots the *WISE* colors of the final classified sample, the $W2 - W3$ colors of the non-AGNs tend to be significantly redder than the Type-1 sources and slightly redder than the Type-2 sources. Their colors overlap the ULIRG space (Figure 1) and thus may contain AGNs that are so heavily obscured that their emission signatures are absent from their optical and near-infrared spectra.

4.3. Final Accounting

The full sample of astrophysical objects that obey our selection criteria amounts to 209 objects: 169 identified spectroscopically with SDSS (listed in Table 3) and 40 objects supplemented by us (listed in Table 1). For five of the candidates, we only have redshifts and classifications from the literature. One ULIRG, W2M J0354+0037, originally identified in Strauss et al. (1992), is classified as a LINER in Veilleux et al. (2009), which we count as a Type-2 QSO. Another object, W2M J0347+0105, is a Seyfert 1.5 galaxy (i.e., QSO in our classification) from Boroson & Green (1992). W2M J0338 +0114 is classified as a Seyfert 2 galaxy (i.e., QSO-2) in Huchra et al. (1999). W2M J2305+0011 is a nearby ($z = 0.025$) galaxy also found in Huchra et al. (1999). Ws82 J2305−0039 is a hyperluminous dust-obscured AGN (Hot DOG; Tsai et al. 2015), which we count as a red Type-1 AGN. We also recover a FIRST-2MASS red Type-1 AGN, F2M2216−0054, from Glikman et al. (2007), for which we had a previously obtained spectrum.

The total sample of 40 QSO candidates that lack SDSS spectra breaks down into the following classifications (including those from the literature): 24 Type-2 QSOs, 7 red QSOs,

8 galaxies (starburst and quiescent, including the source in the Appendix), and 1 Type-1 QSO. We merge this sample with the corresponding SDSS-identified sample of QSOs (Section 3.1) for a full analysis of the luminous, obscured, infrared-selected QSO population.

The breakdown of the final source classification for the entire sample is shown in Table 4: 147 AGNs, of which 57 are Type-1 unobscured QSOs, 69 are Type-2 AGNs, and 21 are reddened Type-1 quasars (see Section 5.1); the remaining 62 do not show AGN activity in their optical or near-infrared spectra. Numbers in parentheses are the subset of each category coming from our follow-up spectroscopy. We note that while SDSS is highly effective at finding blue Type-1 AGNs, ∼35% of obscured sources (both Type-2 and red Type-1) are missed by SDSS and recovered in this work. This is crucial, as many red quasar studies have been conducted out of the SDSS spectroscopic sample, noting unusual and extreme properties of the red quasars found therein (e.g., Richards et al. 2003; Ross et al. 2015; Hamann et al. 2017; Tsai & Hwang 2017). Those obscured sources are likely just the tip of a population that may be significantly larger.

In Figure 9 we plot the full sample, divided by source classification, on the same *WISE* color–color axes as in Figure 1. Blue Type-1 AGNs (blue circles) occupy bluer $W2 - W3$ colors, with red Type-1 AGNs (red crosses) largely overlapping but with slightly redder colors and larger scatter. Type-2 AGNs (green triangles) are found at redder $W2 - W3$ colors, and, as noted in Section 4.2, objects without clear AGN signatures (orange squares) are redder still. Figure 10 shows the redshift histograms for the four classes of objects, binned by $\Delta z = 0.2$. As expected, Type-1 AGNs (blue and red) reach the highest redshifts, while Type-2 AGNs and non-AGNs are seen

only as far as $z < 1$ because their optical emission is dominated by starlight.
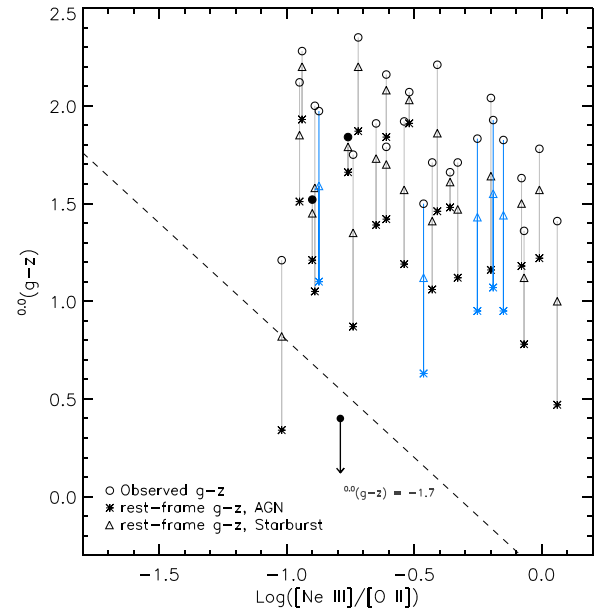
5. Results

5.1. Reddened Type-1 QSOs

As Lacy et al. (2007) and Lacy et al. (2013) have shown, an unbiased, infrared-selected quasar sample will contain both normal Type-1 AGNs and reddened Type-1 AGNs similar to those found by, e.g., Glikman et al. (2012). To identify the reddened quasars among our broad-line subsample, we fit a reddened quasar composite template to all the Type-1 QSOs with SDSS spectra, following the procedure outlined in Glikman et al. (2007) and Glikman et al. (2012).

Figure 11 plots the distribution of $E(B - V)$ for the broad-line QSOs binned by 0.1 mag and shows that the majority of quasars in this sample are unreddened. Figure 12 shows four example unreddened spectra (black line) spanning the redshift range of our sample, with the best-fit template at the stated reddening plotted on top (red line). This figure demonstrates the appropriateness of fitting the spectra with a QSO template as has been done for more heavily reddened QSOs. We note that because unreddened QSOs have an intrinsic distribution in the spectral index of their optical/UV continua (as shown by Richards et al. 2003), some of the reddening fits will return a negative $E(B - V)$, which is likely the result of trying to fit an average QSO spectrum to a very blue QSO.

Following Lacy et al. (2007), we define a reddened QSO as having $E(B - V) > 0.25$, consistent with the sharp drop in the $E(B - V)$ histogram. Based on this criterion, there are 14 red Type-1 AGNs among the objects with SDSS spectra. Adding to these the seven newly discovered red Type-1 AGNs brings their total number to 21. As described in Section 3.2.1, we obtained near-infrared spectra for 11 of these, extending their wavelength coverage.

Figures 13(a) and (b) show the optical through near-infrared spectra, sorted by decreasing redshift, of the 14 red QSOs found in SDSS, along with six of the seven[20] that were added by our own spectroscopy. We overlay the best-fit reddened QSO template with an orange line.[21] To investigate whether the near-infrared spectra that we obtained (Section 3.2) are consistent with the expected shape based on the reddened template, we scaled the near-infrared spectra to the effective fluxes in the four UKIDSS near-infrared bands (green circles). We do this by shifting the mean pixel value in the near-infrared spectrum (excluding regions of atmospheric absorption) to the mean effective flux of the four UKIDSS bands. We also plot the fluxes based on SDSS photometry with violet circles, scaling the non-SDSS spectra to the optical photometry. This allows us to compare what the reddened template predicts for the near-infrared spectroscopy to what we actually see.

We see that while the data generally agree in many of the objects, in some cases the near-infrared spectrum varies significantly from what would be expected based on the reddened QSO template. Objects such as W2M2255+0049, W2M2346−0038, W2M0251−0048, F2M0156−0058, and F2M0036−0113 show an excess of near-infrared emission compared to the reddened template that fits the optical

---

[20] The spectrum for Ws82 J2305−0039, the Hot DOG, is proprietary, and we do not show it.

[21] The reddened QSO template fitting was performed only on the optical spectrum for consistency with the $E(B - V)$ shown in Figure 11.

Figure 8. Rest-frame $(g - z)$ color vs. [Ne III]/[O II] of sources for which we obtained spectra (black symbols) and higher-redshift sources with SDSS spectra lacking Hα and [N II] (blue symbols). This parameter space, defined by Trouille et al. (2011), is intended to separate AGNs from starbursts when sources' redshifts make Hα and [N II] inaccessible. We plot the observed $(g - z)$ color with circles (filled circles are the sources in the star-forming region of Figure 7) and plot the k-corrected rest-frame colors using a starburst template (triangles) and a Type-2 AGN template (asterisks) to represent the range of rest-frame $(g - z)$ colors that a source may have. The dashed line is the boundary defined by Trouille et al. (2011) with AGNs at the upper right. Nearly all our sources are found in the AGN region of the diagram. However, one source, Ws82 J0220+0033 (marked with a filled circle and a downward-pointing arrow), appears well outside the plotted range in the star-forming region of the diagram.

spectrum well. Other sources, such as W2M J2046+0023, W2M J0256+0113, and W2M J0253+0001, show a difference between the near-infrared spectrum and both the reddened template and the photometric fluxes. Only one of these, W2M J2046+0023, is weakly detected in the FIRST catalog, with a 1.4 GHz flux density of 1.1 mJy, and none of these sources are detected in X-rays (Section 5.2.1); hence, variability due to beaming is unlikely. A change in the reddening, intrinsic luminosity, and/or accretion rate may explain these discrepancies, but would require monitoring of these sources to investigate this hypothesis. Table 5 lists the 21 reddened quasars and their measured parameters.

To account for the fraction of broad-line QSOs that obey our selection criteria, we sum all the broad-line QSOs for a total of 57 Type-1 and 21 red Type-1 quasars. The 21 red quasars with $E(B - V) > 0.25$ thus make up 27% of the broad-line QSOs brighter than 20 mJy at 22 μm. Note that we do not need to account for flux losses due to obscuration in the mid-infrared, because even when shifted to the rest frame only ∼2% of the intrinsic flux is lost (compared with ∼60% in g band). This amounts to less than 0.05 mag reduction in brightness for all the sources (compared with ∼1 mag in g band) and means that if a mid-infrared flux limit is considered, rather than optical or near-infrared, the fraction of red quasars is simply the ratio of reddened to total Type-1 quasars. This fraction is also borne out in our luminosity function (LF) analysis discussed in Section 5.3.

Table 2
Line Diagnostics

Object (Name)	$\log([\text{O III}]/\text{H}\beta)$	$\log([\text{N II}]/\text{H}\alpha)$	$\log([\text{Ne III}]/[\text{O II}])$	$(g-z)_{\text{AB}}$[a] (mag)
Ws82 J0021+0038	1.19	−0.27	−0.08	1.63
W2M J0030−0027	0.91	−0.23	−0.72	2.35
W2M J0103−0055	1.13	⋯	−0.07	1.36
Ws82 J0150−0108[b]	−0.24	⋯	−1.02	1.21
Ws82 J0213−0057	1.20	−0.51	−0.01	1.78
Ws82 J0220+0033[c]	0.70	−1.25	−0.79	−1.70
Ws82 J0228−0054	1.04	⋯	0.06	1.41
Ws82 J0253−0046	−0.13	−0.49	−0.90	1.52
W2M J0306+0108	1.73	−0.59	−0.61	2.16
W2M J0307−0019	0.87	−0.71	−0.33	1.71
W2M J0349+0054	1.41	−0.02	−0.52	2.07
Ws82 J2052−0108	0.16	⋯	−0.43	1.71
Ws82 J2054+0041	0.74	−0.40	−0.94	2.28
W2M J2057+0054	1.03	⋯	−0.41	2.21
Ws82 J2110−0101	1.24	−0.52	−0.36	1.66
Ws82 J2148−0011	2.11	⋯	−0.89	2.00
Ws82 J2201−0038	1.28	⋯	−0.20	2.04
W2M J2216+0058	0.36	−0.24	−0.61	1.79
Ws82 J2223+0113	0.39	⋯	−0.65	1.91
Ws82 J2240+0030	0.46	⋯	−0.95	2.12
W2M J2246+0103	−0.10	−0.53	−0.76	1.84
Ws82 J2330−0012	0.83	−0.27	−0.74	1.75
Ws82 J2343−0059	1.06	⋯	0.43	2.18
W2M J2355−0114	0.66	⋯	−0.54	1.92
Ws82 J0056+0032	0.87	⋯	−0.25	1.83
Ws82 J0107−0053	0.63	⋯	−0.87	1.97
Ws82 J0244−0056	0.91	⋯	−0.15	1.83
W2M J0336−0007	0.93	⋯	−0.19	1.93
Ws82 J2335−0050	0.73	⋯	−0.46	1.50

Notes. Objects in the lower part of the table are from the sample with SDSS spectra and appear as blue symbols in Figure 8.
[a] These are the observed $(g-z)$ colors, shown as a circle in Figure 8. The rest-frame, k-corrected $^{0.0}(g-z)$ colors are shown in the figure.
[b] This object appears on the boundary of the star-forming region of the TBT diagram and has the lowest $[\text{O III}]/\text{H}\beta$ ratio in this sample. We classify this source as a galaxy.
[c] This object appears in the star-forming region of both BPT and TBT diagrams.

(This table is available in machine-readable form.)

Table 3
WISE-Selected AGN Candidates in Stripe 82 with SDSS Spectroscopy

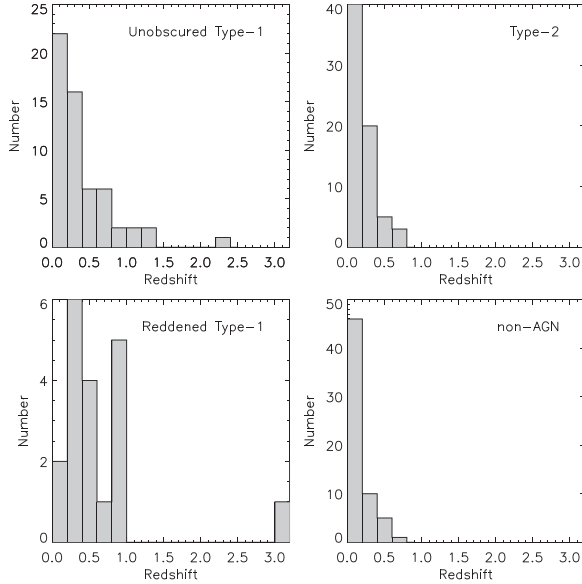| Name	g[a] (mag)	r[a] (mag)	i[b] (mag)	J[b] (mag)	K[b] (mag)	$W1$[b] (mag)	$W2$[b] (mag)	$W3$[b] (mag)	$W4$[b] (mag)	Redshift	Class[c]
W2M J001741.75+000752.3	16.67	16.01	15.61	15.48	14.30	12.86	11.57	7.76	5.08	0.070	QSO-2
W2M J002831.69−000413.0	18.11	17.71	17.39	15.96	14.14	12.47	11.56	8.85	6.54	0.252	QSO
W2M J002944.90+001011.1	16.75	16.25	15.83	15.45	14.34	13.05	11.97	7.97	5.27	0.060	QSO-2
W2M J003431.74−001312.7	18.07	18.07	18.07	16.65	15.21	13.68	12.50	9.07	6.36	0.381	QSO
W2M J003443.48−000226.8	16.18	15.41	14.95	15.00	13.56	11.91	10.14	6.53	3.86	0.042	QSO-2
W2M J003659.82−011332.5	21.29	20.19	19.66	16.57	13.63	11.67	10.51	7.88	5.21	0.294	red-QSO

Notes.
[a] AB magnitudes.
[b] Vega magnitudes.
[c] The classifications listed in this column are based on our analysis described in Section 4 of the text.

(This table is available in its entirety in machine-readable form.)
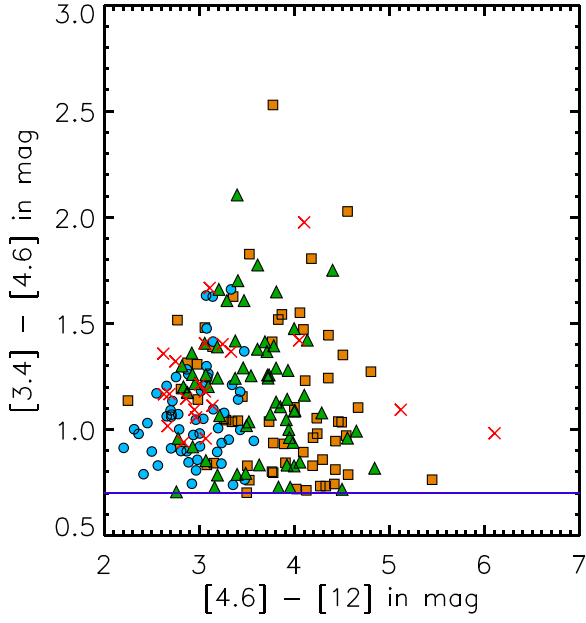
Figure 9. *WISE* infrared colors of the final, complete sample focusing on the selection region, as shown in Figure 1, with the horizontal violet line representing the $W1 - W2$ cut. Blue circles are Type-1 AGNs, green triangles are Type-2 AGNs, red crosses are the red Type-1 AGNs, and orange squares are the non-AGNs.
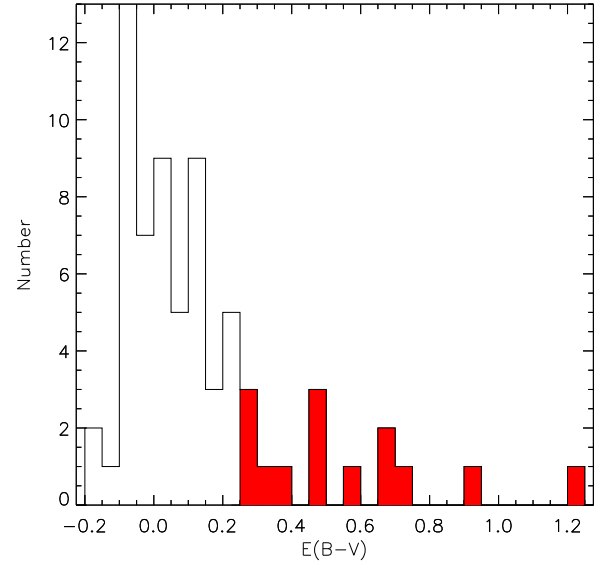

Figure 11. Reddening histogram for the broad-line quasars with SDSS spectra obeying our infrared selection. The red shaded bins represent 11 Type-1 reddened quasars with $E(B - V) \geqslant 0.25$ mag.

Figure 10. Redshift distributions for the four classes of objects from our survey.
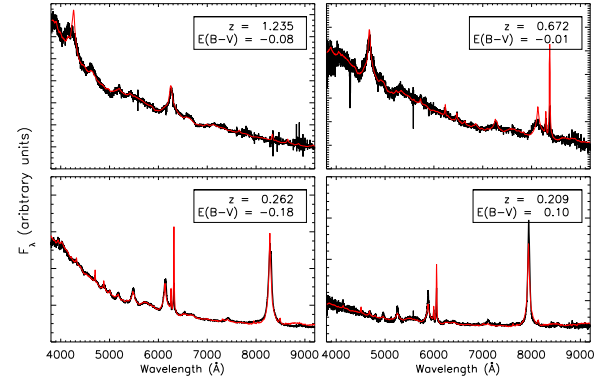
Figure 12. Four example spectra of unreddened quasars from our sample at a range of redshifts (shown in the legend), with the best-fit reddened template overplotted with a red line.

Table 4
Final Accounting of Sources in Our Sample

AGNs (147)			Non-AGNs
Type-1	Red Type-1	Type-2	Galaxies
57 (1)	21 (7)	69 (24)	62 (8)

Note. Numbers in parentheses indicate the number of sources in the category that are newly identified in Table 1.

Consequently, we find at the brightest infrared flux limit that the fraction of red quasars is consistent with, though somewhat higher than, the ~20% found via radio plus infrared selection in our previous studies (Glikman et al. 2007, 2012), which assumed that the radio properties of red QSOs are independent of their reddening properties. To first order, at the bright end, it appears that this assumption is acceptable. Furthermore, if red QSOs are a phase in a merger-driven scenario of coevolution, as argued in Glikman et al. (2012), then the duration of the phase determined in that work remains ~20%, but could be as high as ~30%, of the blue QSO lifetime.

5.2. X-ray Properties

5.2.1. X-ray Observations

An advantage of conducting a survey in Stripe 82 is the access to the rich multiwavelength data that exist in that region of the sky. The Stripe 82X survey combines all archival observations from

15
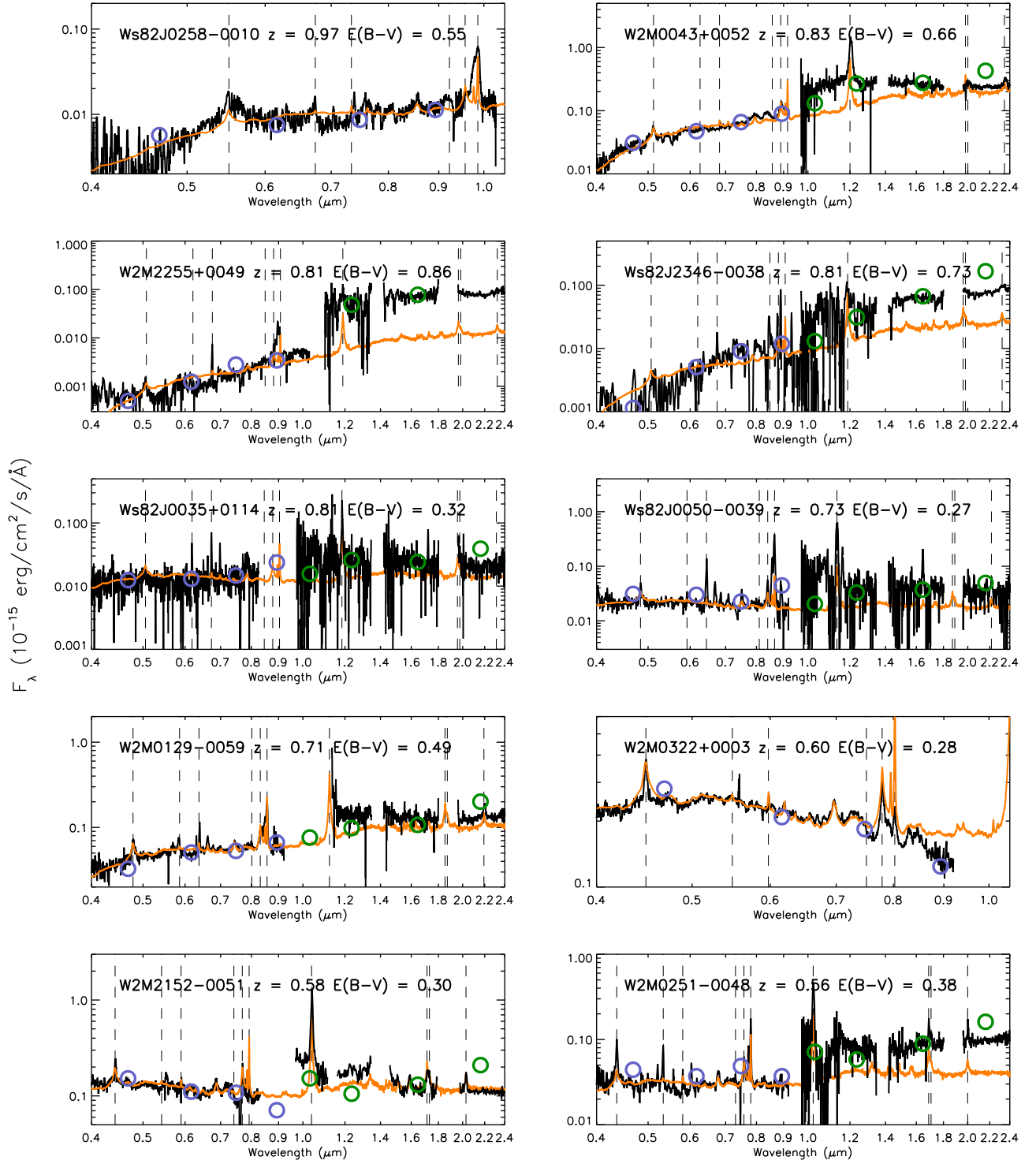
(a)

Figure 13. (a) Spectral atlas of the 20 reddened QSOs in our sample for which we have spectra. They are defined as having $E(B-V) > 0.25$ based on a reddened QSO template fit to the optical spectrum (orange line). When a near-infrared spectrum is available, we scale it to the UKIDSS photometry (green circles) and plot it in an expanded wavelength range. We also plot the SDSS photometry with violet circles for a full comparison of photometric SED and spectroscopic information. Although there is broad agreement in the optical, the near-infrared spectra, photometry, and reddened template often diverge, suggesting an incomplete understanding of the emission from red QSOs in this part of the spectrum, or else strong source variability. (b) Same as panel (a).

Chandra and *XMM* (LaMassa et al. 2013a, 2013b) plus targeted observations from *XMM*, amounting to a total of 31.3 deg^2 down to a flux limit of $\sim 10^{-15}$ erg s^{-1} cm^{-2} (0.5–10 keV; LaMassa et al.

2016c). A total of 34 of our sources overlap the X-ray area of Stripe 82X. We use X-ray detections for these sources to study their obscuration via their hardness ratios (HRs) and examine

16
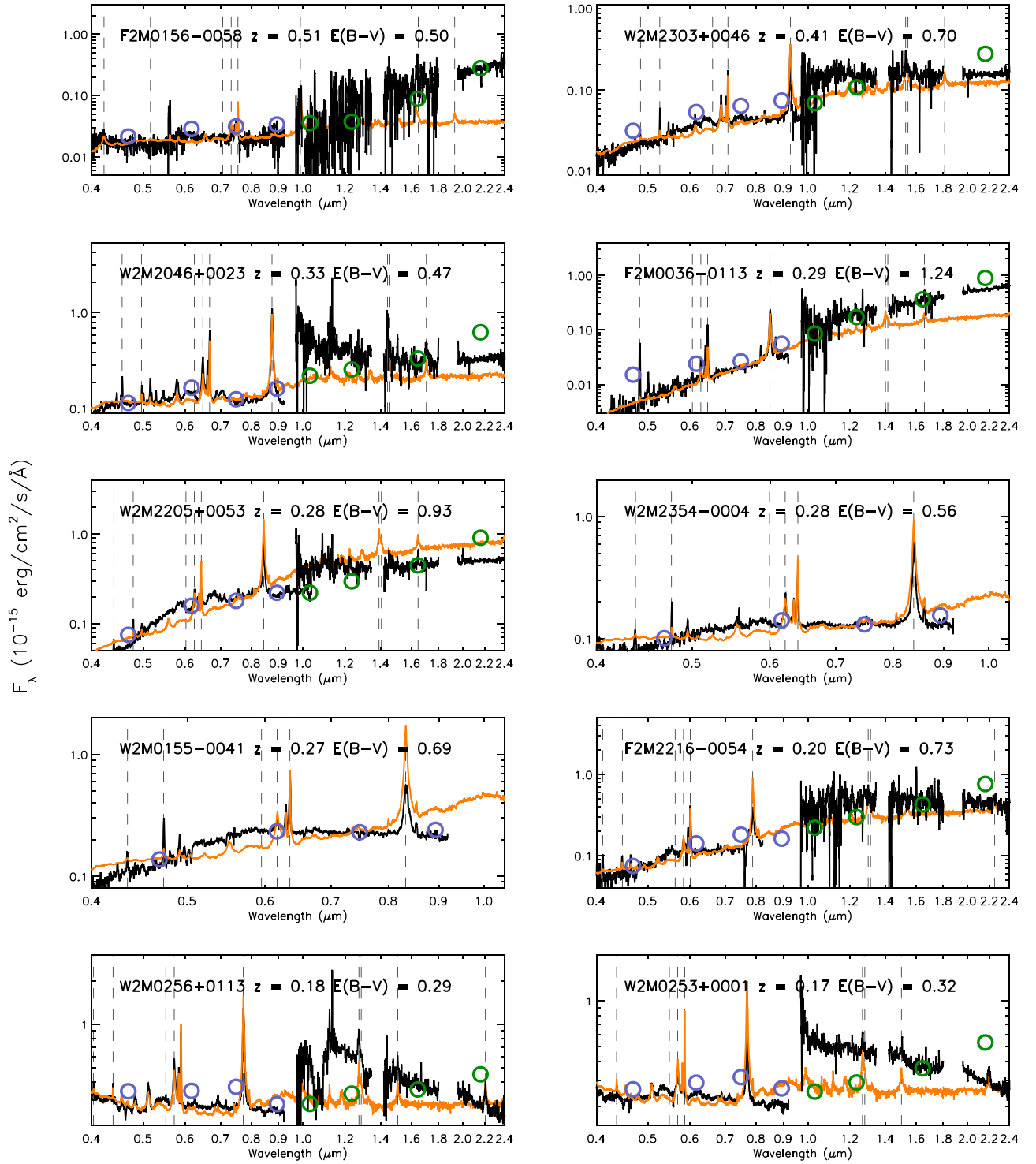
(b)

Figure 13. (Continued.)

where these sources lie with respect to known relations between rest-frame hard X-ray (2–10 keV) luminosity and rest-frame luminosity at 6 μm, as well as [O III] line luminosity.

We cross-matched our sample of AGNs with the Stripe 82X catalog and found X-ray counterparts for 10 sources, 7 from

XMM observations and 4 from *Chandra*. One X-ray source, W2M J2330+0000, was found in an overlapping area covered by both observatories. Interestingly, this object was found to have line ratios consistent with a star-formation-dominated source in all three diagnostics, as well as hydrogen emission

Table 5
Reddened QSO Properties

Name	Redshift	$E(B-V)$ (mag)	A_V (mag)	Spectrum
J2305−0039	3.106	…	…	Tsai et al. (2015)
Ws82 J0258−0010	0.969	0.55	3.66	LRIS
W2M J0043+0052	0.828	0.66	3.96	SDSS/TSpec
W2M J2255+0049	0.812	0.86	5.14	Kast/SpeX
Ws82 J2346−0036	0.810	0.73	4.37	SALT[a]/SpeX
Ws82 J0035+0114	0.805	0.32	1.91	Kast/TSpecP200
Ws82 J0050−0039	0.728	0.27	1.53	SDSS/TSpecP200
W2M J0129−0059	0.710	0.49	2.73	SDSS/TSpec
W2M J0322+0003	0.603	0.28	1.45	SDSS
W2M J2152−0051	0.582	0.30	1.56	Kast/SpeX
W2M J0251−0048	0.559	0.38	1.95	SDSS/TSpecP200
F2M0156−0058	0.506	0.50	2.44	SDSS/SpeX
W2M J2303+0046	0.412	0.70	3.23	SDSS/TSpec
W2M J2046+0023	0.332	0.47	2.06	SDSS/TSpec
F2M0036−0113	0.294	1.24	5.26	SDSS/TSpec
W2M J2205+0053	0.285	0.93	3.92	SDSS/TSpec
W2M J2354−0004	0.279	0.56	2.34	SDSS
W2M J0155−0041	0.269	0.69	2.90	SDSS
F2M2216−0054	0.200	0.73	2.90	Kast/SpeX
W2M J0256+0113	0.177	0.29	1.13	SDSS/TSpecP200
W2M J0253+0001	0.171	0.32	1.22	SDSS/TSpec

Note.
[a] We obtained a spectrum of this source with LRIS, from which we determined the source redshift. However, the LIRS spectrum was affected by a bad column, affecting the continuum shape. Therefore, we use the lower-signal-to-noise SALT spectrum for determining $E(B-V)$.

(This table is available in machine-readable form.)

line widths ∼600 km s^{-1}, and thus was classified as a galaxy and not an AGN.[22] In addition, its hard X-ray counts from *Chandra* were too low for a reliable luminosity estimate. We therefore do not consider the duplicate *Chandra* data further.

We also observed five additional sources that obeyed our color selection with *Chandra* using Guaranteed Time Observations (GTO; PI Murray). We processed the raw data using the standard data processing script chandra_repro, which is part of *Chandra*'s custom data analysis software, *Chandra* Interactive Analysis of Observations (CIAO). This initial reprocessing accounts for cosmic rays, known background events, varying pixel sensitivities, and dust accumulation on the CCD chip. The reprocessing script produces a level-two events file, from which we identified the source detections by their original target coordinates. Four sources had clear detections (>10 counts at their original source coordinates), while one source, W2M J0156−0058,[23] was not detected in a 6 ks observation. After identifying a source, we measure its flux within a 5″-diameter circular region centered on the detection. We determine the background from an annulus around the source region, with an inner diameter of 10″ and an outer

diameter of 30″. Table 6 provides details on the GTO observations.

We measured the hard X-ray flux in the rest-frame 2–10 keV energy band using the CIAO tool srcflux. Because the corresponding observed-frame energy band (∼1.6–8 keV at redshift 0.2) is within *Chandra*'s sensitivity range, we do not use a *k*-correction for our flux measurements, as these rely on assumptions about the spectral index, and instead measure the flux directly from the data in the appropriate range corresponding to rest-frame 2–10 keV. Table 7 reports the X-ray properties of all 14 sources with X-ray detections.

The *Spitzer*-based study of Lacy et al. (2013, 2015), upon which this survey expands, found X-ray counterparts for ∼22% of their sample in archival catalogs. Similar to our finding of an emission-line galaxy with a strong X-ray detection, Lacy et al. (2013) find such sources in their sample. This emphasizes the fact, which has been noted elsewhere (e.g., Eckart et al. 2010, and references therein), that while some AGN-detection methods may be more complete and efficient than others, there has yet to be a single selection technique that can recover all AGNs.

5.2.2. Hardness Ratios

We compute HRs for all X-ray-detected sources to further characterize the sample population through comparison with other quasars (e.g., Gallagher et al. 2005) and to explore a possible correlation with reddening. The HR of an X-ray source provides a crude estimate of the X-ray absorption, when there are insufficient counts for X-ray spectral analysis. HRs are computed by the equation $(H-S)/(H+S)$, where H and S represent the net counts in the hard and soft bands, respectively. We define the soft X-ray band as 0.5–2 keV and the hard band as 2–10 keV. For computing HRs in the GTO data, we use the CIAO tool dmcopy with the appropriate energy filters, to make raw files containing only soft or hard counts. We then use dmextract, with the previously mentioned aperture regions, to find total soft, hard, and overall counts. Due to our relatively low counts, we calculate HRs using Bayesian Estimation of Hardness Ratios (BEHR; Park et al. 2006).

We also determine HRs for the sources from Stripe 82X. LaMassa et al. (2016a) computed HRs for X-ray-selected AGN candidates obeying the color cut $R - W1 > 4$ in the Stripe 82X catalog. Those measurements were done using BEHR, and we find matches to three sources in our sample. We computed HRs for the remaining six objects using the counts provided in the Stripe 82X catalog and the aforementioned equation.[24] Together, we have 13 X-ray measurements for our infrared-selected sample, 12 of which we classified as AGNs and one as a galaxy.

Figure 14 shows the HRs of our X-ray-detected sources, as compared with X-ray-detected AGNs in Stripe 82 from LaMassa et al. (2016a). Comparing the mean HRs by type, we see the expected behavior where objects classified as Type-1 unobscured QSOs have a mean HR of −0.63, consistent with the average of −0.63 for radio-quiet quasars with $\Gamma_{2-10} = 2.0$ reported by Gallagher et al. (2005). The three red QSOs have an average HR of 0.47, and Type-2 AGNs have similarly hard

---

[22] However, this source's uncorrected X-ray luminosity is found to be ∼8 × 10^{42} erg s^{-1}, well into the AGN-luminosity regime. Nonetheless, we do not include this source in our AGN sample since our other criteria were applied uniformly to all sources, and we do not possess X-ray fluxes for all the sources in our IR-selected sample.
[23] This object is a known red quasar, reported previously by Urrutia et al. (2009), Glikman et al. (2012), and Glikman et al. (2013).

[24] BEHR was developed to properly account for HRs in the low-count regime and in cases of nondetections in a given band and approaches the same result as the equation in the high-count limit. Most of the detections have >20 counts in the soft and hard bands, making our use of the direct formula acceptable.

Table 6
Summary of *Chandra* GTO Observations

Name (J2000)	Redshift	Class	ObsID	Exposure (s)	Total counts
W2M J0156−0058	0.506	redQSO	16273	5990	⋯
W2M J0306+0108	0.189	QSO-2	16267	9937	95
Ws82 J2054+0041	0.203	QSO-2	16269	1147	56
W2M J2355−0114	0.323	QSO-2	16272	8949	44
W2M J2216−0054	0.200	redQSO	16274	5001	84

spectra with a mean HR of 0.48, though the red QSOs have much redder $R - W1$ colors. This substantial X-ray spectral hardening is broadly consistent with increasingly strong attenuation of soft X-rays by the obscuring medium. However, we note that the use of HRs as proxies for obscuration is redshift dependent, as shown in LaMassa et al. (2016a, Figure 19). Within the blue Type-1 and Type-2 subgroups, the redshifts are within a relatively small range ($\Delta z \lesssim 0.5$ and 0.3, respectively), while three of the four red Type-1 AGNs are all around $z \sim 0.8$, with one source at $z = 0.2$. Conclusions drawn from this analysis are intended to be illustrative of the actual obscuration, which would require significantly more counts for a proper X-ray spectral analysis.

5.2.3. Luminosity Relations

Bolometric luminosities for AGNs are important to accurately determine their Eddington ratios ($L/L_{\rm Edd}$), which inform us about their accretion rates. Because optical wavelengths are strongly affected by dust extinction, bolometric corrections (e.g., Richards et al. 2006) derived from those wavelengths are highly uncertain. Thus, determining bolometric luminosities of obscured AGNs requires reddening-insensitive bands such as hard X-rays, mid-infrared, or some other isotropic luminosity indicators such as [O III] line flux. While the aforementioned indicators are well calibrated for local AGNs and optically selected Type-1 quasars, it is unclear whether they extend to infrared-bright and obscured sources such as our *WISE*-selected AGNs at $z > 1$.

The luminosity of the [O III] λ5007 line and its correlation with hard X-ray luminosity are considered important probes of intrinsic luminosity, because all these diagnostics are thought to emit isotropically (Heckman et al. 2005; LaMassa et al. 2009, 2011; Jia et al. 2013). We use [O III] λ5007 fluxes for our Type-2 sources from the GANDALF fits (Section 4.1) and by fitting individual Gaussians, or de-blending Hβ + [O III] complexes when necessary, to the Type-1 sources. In Figure 15 we plot log ($L_{\rm [O III]}$) versus log ($L_{X\,2-10\,{\rm keV}}$) for our *WISE*-selected source measurements (colored stars) and compare them with samples of AGNs for which the same has been measured (e.g.; Heckman et al. 2005; Panessa et al. 2006; LaMassa et al. 2010; Jia et al. 2013; Ueda et al. 2015).

Despite their varying amounts of obscuration, our sources mostly lie close to the best-fit line, even though they are 2–3 orders of magnitude more luminous than the Panessa et al. (2006) sample. While these results suggest that the same relationships exist for the *WISE*-selected AGNs as for other large samples of AGNs, the scatter in the relation is sufficiently large that it is suboptimal for determining bolometric luminosities of individual sources.

Another relation worth examining is one correlating X-ray and mid-IR luminosities, which has been established for low-luminosity AGNs at low redshifts (Lutz et al. 2004; Gandhi et al. 2009). We compare the 14 X-ray luminosities in our possession to their rest-frame 6 μm infrared luminosities, determined by interpolating between the *WISE* bands, in Figure 16. The lower-luminosity AGNs do fall on the relation of Lutz et al. (2004; shaded region). However, we see departures from this relation at higher infrared luminosities. To account for this, Stern (2015) derived an updated relation (dot-dashed line) taking into account luminous Type-1 quasars (plotted with black circles). Chen et al. (2017) find a similar luminosity-dependent relation in the form of a bilinear power law (dotted line) based on Type-1 AGN overlapping wide-area X-ray surveys spanning the full X-ray luminosity range shown in the figure.

Nevertheless, we see that the three most luminous QSOs in our sample lie well below even this newer relation. One of these is a blue QSO with an HR indicating negligible absorption, while the other two are reddened Type-1 QSOs whose HRs (-0.085 and 0.321) imply a range of absorptions. LaMassa et al. (2016b) investigated the placement of two F2M quasars observed with *NuSTAR* on this relation. And, combined with another two F2M quasars observed with *XMM*, Glikman et al. (2017) show that at high infrared luminosities red quasars depart from the relations established at low luminosity. We plot these F2M red quasars with red circles, showing the absorption-corrected values with filled symbols. Based on the size of the absorption correction for the F2M sources and the low HR of the most IR-luminous source, we do not expect a corrected L_X to agree with the relation at the highest luminosities.

For additional comparison, we also plot the location of Hot DOGs (Wu et al. 2012), which are heavily obscured hyperluminous infrared galaxies dominated by AGN activity, using the measurements of Ricci et al. (2017a). These sources also lie well below the relation, and systematically below luminous Type-1 quasars by $\sim$0.5 dex. Ricci et al. (2017a) suggest that the Hot DOGs are underluminous in X-rays owing to their potentially very high Eddington ratios ($L/L_{\rm Edd} \sim 1$; Wu et al. 2018) and possible saturation of the X-ray-emitting region of the AGN. F2M red quasars have also been shown to have very high Eddington ratios (Urrutia et al. 2012; Kim et al. 2015), and the same may be the case for the *WISE*-selected sources in this work.

If the X-ray weak interpretation is correct for these AGNs, then their X-ray luminosity may not be a reliable bolometric luminosity indicator. Alternatively, if, by their selection as infrared-bright sources, they have an excess of infrared emission from hot dust ($\sim$500 K peaks at 6 μm), then bolometric corrections for luminous infrared-selected AGNs

Table 7
X-ray Properties of WISE-selected AGNs in Stripe 82

Name (J2000)	Class	z	2–10 keV Hard X-ray flux ($\times 10^{-14}$ erg s^{-1} cm^{-2})	Hard X-ray Luminosity log(erg s^{-1})	Mission	HR	$L_{6\mu m}$ log(erg s^{-1})	$L_{\rm [OIII]}$ log(erg s^{-1})
W2M J0043+0052	redQSO	0.828	8.4 ± 0.8	44.45	*XMM*	−0.085	46.41	…
Ws82 J0050−0039	redQSO	0.728	$8.1^{+9.4}_{-6.8}$	44.30	*Chandra*	0.863	45.20	43.68
W2M J0054+0001	QSO	0.647	<9.5	…	*Chandra*	−0.553	45.80	42.79
Ws82 J0056+0032	QSO-2	0.484	0.5 ± 0.4	…	*XMM*	−0.581	43.21	42.86
W2M J0119−0008	QSO	0.090	30.5 ± 2.1	42.79	*XMM*	−0.732	43.63	40.99
W2M J0139−0006	QSO-2	0.196	38.3 ± 2.5	43.63	*XMM*	0.815	45.23	42.53
W2M J0142+0005	QSO	0.146	44.0 ± 2.6	43.40	*XMM*	−0.651	44.42	41.55
W2M J0149+0015	QSO	0.552	14.9 ± 1.4	44.27	*XMM*	−0.575	45.90	42.98
W2M J0306+0108	QSO-2	0.189	41.2	43.63	GTO	0.897	44.51	41.56
Ws82 J2054+0041	QSO-2	0.203	22.0	43.54	GTO	0.832	44.68	40.44
Ws82 J2255+0049	redQSO	0.812	1.2 ± 0.1	44.57	*Chandra*	0.321	41.65	46.14
W2M J2330+0000	GALAXY	0.122	20.0 ± 3.3	42.90	*XMM*	−0.154	43.95	41.14
…[a]	…	…	<3.1	…	*Chandra*	…	…	…
W2M J2355-0114	QSO-2	0.323	9.47	43.51	GTO	0.450	45.27	41.84
W2M J2216-0054	redQSO	0.200	52.0	43.75	GTO	0.792	44.86	41.95

Note.

[a] This entry is a duplicate detection of J233032.94+000026.5.

(This table is available in machine-readable form.)
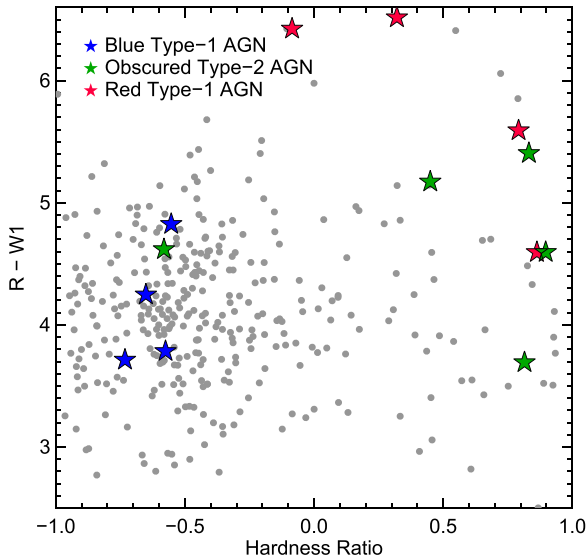
Figure 14. HRs vs. $R - W1$. WISE-selected AGNs in Stripe 82 with X-ray detections are represented by the following symbols: blue stars are Type-1 QSOs, green stars are Type-2 QSOs, and red stars are reddened Type-1 QSOs. For comparison, we show X-ray-detected AGNs in Stripe 82 with $z < 1$ from LaMassa et al. (2016a) (gray circles, similar to their Figure 20). The *WISE*-selected red Type-1 AGNs are among the reddest in $R - W1$. Both Type-2 and red Type-1 AGNs have harder X-ray spectra, with red Type-1 sources also having redder colors.

using an infrared wavelength may overestimate their bolometric luminosities and thus their accretion rates and (to a lesser extent) black hole masses.

5.3. The Evolution of the AGN Mid-IR Luminosity Function

With a complete sample of carefully selected, well-defined AGNs in hand, we are now able to investigate the evolution of QSOs, separated by their obscuration type, across luminosities and redshifts. To do so, we append to our sample the sources from Lacy et al. (2013), which covered *Spitzer* fields of various areas and depths and identified 527
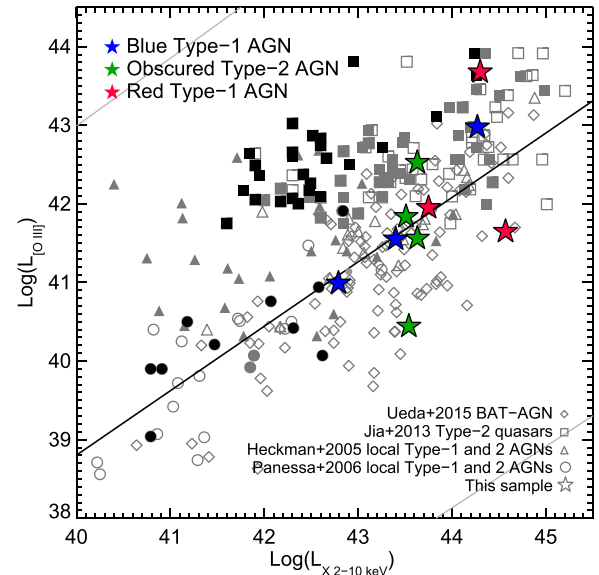
Figure 15. [O III] luminosity vs. hard X-ray luminosity (in the 2–10 keV observed energy range) for our *WISE*-selected sources. Blue stars are Type-1 QSOs, green stars are Type-2 QSOs, and red stars are reddened Type-1 QSOs. For comparison we plot the same for AGNs from various samples with gray and black symbols. Diamond symbols are measurements from the hard-X-ray-selected, local *Swift*-BAT AGNs (Ueda et al. 2015), squares are Type-2 quasars from SDSS reaching out to $z \sim 0.7$ (Jia et al. 2013), and triangles are a sample of local Type-1 and Type-2 AGNs (Heckman et al. 2005; Panessa et al. 2006). Filled gray symbols are Type-2 AGNs, while open symbols are either Type-1 AGNs or obscured AGNs whose X-ray luminosity has been absorption corrected. The black filled symbols are Compton-thick sources identified in the respective samples. The black line represents the best-fit correlation between $\log L_{\rm [OIII]}$ and $\log L_{X\,2-10\,\rm keV}$ for the Panessa et al. (2006) sample.

AGNs using slightly modified infrared color cuts developed by Lacy et al. (2007). These AGNs were found out to $z \gtrsim 4$ and spanned $\sim$1.5–2 orders of magnitude in luminosity at a given redshift. However, the relatively limited survey area of 54 deg^2 meant that the most luminous systems were missing. Figure 17 shows how the wide area covered by our survey,
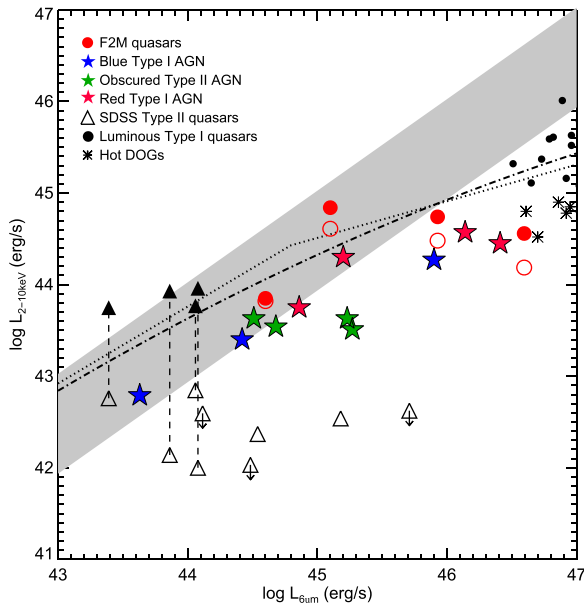
Figure 16. Rest-frame 6 μm luminosity vs. rest-frame X-ray luminosity for the AGNs in our sample (star symbols, as described in the legend), which have not been corrected for absorption. For comparison, we plot four F2M red quasars (red circles) analyzed in LaMassa et al. (2016b) and Glikman et al. (2017). Type-2 quasars from SDSS are shown with triangles. Open symbols show the uncorrected X-ray luminosities, and filled symbols are absorption-corrected luminosities. The shaded region represents a relation between the two wavelengths derived from local Seyfert galaxies (Lutz et al. 2004). The dot-dashed line is the relation derived for luminous quasars derived by Stern (2015), which is more applicable to the sources in this work. A similar turnover at high luminosities is seen in the relation derived by Chen et al. (2017) (dotted line). At low luminosities our sources fall on the relation; however, more luminous systems lie below both relations and are possibly underluminous in X-rays.

albeit to shallower depths, complements the Lacy et al. (2013) survey and enables us to sample the large volumes needed to recover the high-luminosity end of the quasar LF (QLF).

Figure 18 shows the combined sample of AGNs from Lacy et al. (2013, 2015) and the current work in luminosity versus redshift space. Large symbols are sources from this work, and small symbols are the sources from Lacy et al. (2015). As in Figure 1 of Lacy et al. (2015), we plot the rest-frame luminosity density at 5 μm, $L_{5\mu m}$, which samples well the intrinsic AGN emission at a wavelength that is minimally affected by obscuration. As was done in Lacy et al. (2015), $L_{5\mu m}$ was determined via SED fitting following an identical procedure (with the exception that *WISE* photometry was used in place of *Spitzer* photometry). The sources added from Stripe 82 broaden the luminosity range to span ~2–2.5 orders of magnitude, reaching the sought-after high-luminosity regime across the redshift range of the survey, and particularly at $z < 1$.

Lacy et al. (2013, 2015) investigated the evolution of the fractions of blue Type-1, red Type-1, and Type-2 AGNs and their luminosity dependence at rest frame 5 μm by fitting the double power-law function,

$$\phi(L, z) = \frac{\phi^*}{(L/L^*)^{\gamma_1} + (L/L^*)^{\gamma_2}}, \qquad (4)$$

characterized by a faint-end slope, γ_1, a bright-end slope, γ_2, and a break luminosity, L^*, where the faint and bright ends

reverse dominance. The function is normalized by the space density, ϕ^*. In addition, the cosmological evolution of the function is fit by the parameterization,

$$\log_{10} L^*(z) = \log_{10} L_0^* + k_1 \epsilon + k_2 \epsilon^2 + k_3 \epsilon^3, \qquad (5)$$

where $\epsilon = \log_{10}((1 + z)/(1 + z_{ref}))$ with $z_{ref} = 2.5$.

The Lacy et al. (2015) study found similar results to studies of X-ray-selected samples: at low redshifts ($z < 1$) and luminosities ($L < L^*$) the obscured fraction decreases rapidly with increasing luminosity, with only a weak dependence on redshift (e.g., Treister & Urry 2005; Treister et al. 2006). However, at high redshifts and luminosities, where X-ray surveys are too small in area to constrain the bright end of the LF, Lacy et al. (2015) found a surprisingly high incidence of luminous, dust-reddened quasars. Whether this trend is principally driven by luminosity or redshift, however, was unclear. As Figure 17 shows, the range in flux limits for the *Spitzer* samples spans only a factor of 15 and covers too small a volume, thus excluding high-luminosity, low-redshift objects. The AGNs found in this current work supplement the sample of fainter AGNs to probe a broader luminosity range at each redshift.

We compute LFs for the three AGN subsets, combining our sample with that of Lacy et al. (2013) and following the identical procedure of Lacy et al. (2015), using a model described by Equations (4) and (5), to compare their shapes and evolutions across redshifts and the full luminosity range. Figure 19 shows the resultant LF as it evolves over four redshift bins: $0.05 < z < 0.4$, $0.4 < z < 0.9$, $0.9 < z < 1.6$, and $1.6 < z < 2.5$. The binned space densities of the different quasar populations are shown with the same symbols as in Figure 18, with black crosses representing the combined space density of all AGN types in the bin. We also show with cyan crosses the "maximal LF," which assumes that all sources are AGNs, including the 62 sources that failed our initial classification criteria (Section 4.1). We note that despite somewhat different color selections of Lacy et al. (2013, 2015) and this work, both methods are highly complete, recovering all luminous quasars in the former (Figure 1 of Lacy et al. 2004) and 94% (97%) of SDSS (red) quasars in this work (Figure 1). Thus, the different selections will not have a significant effect on our results.

The dashed lines are the best-fit QLFs for each AGN type, color-coded accordingly and shown at the mean redshift of each panel (0.225, 0.65, 1.25, 2.05). Table 8 reports on the best-fit parameters to the LF and its evolution (Equations (4) and (5)). These values have changed somewhat from those derived from the deeper fields of Lacy et al. (2015) and demonstrate the importance of sampling the full luminosity range of a population.

Consistent with the earlier results of Lacy et al. (2015), we find that the three classes of QSO populations evolve differently. Figure 20 shows the evolution of the characteristic break luminosity, L^*, as a function of redshift for the three QSO types. Since objects at L^* are responsible for emitting most of the light from a given population, we see that L^* for red QSOs peaked at high redshift and have declined to the present day. Lacy et al. (2015) speculate that this trend is consistent with red QSOs being related to gas-rich galaxy mergers (as has been noted previously;
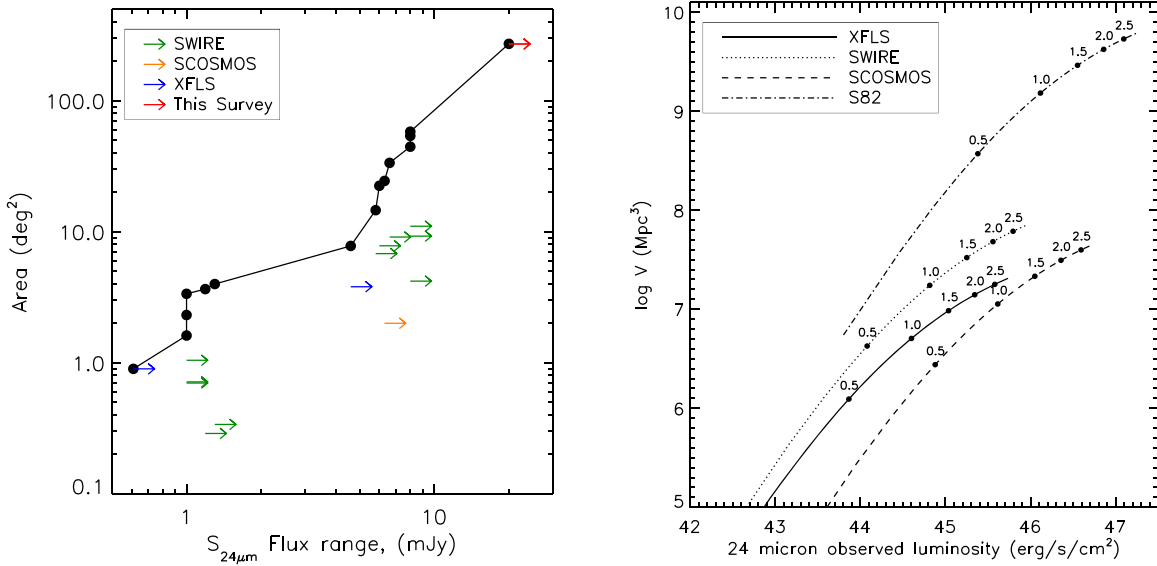
Figure 17. Left: cumulative area vs. flux diagram showing the cumulative area covered by the mid-IR AGN survey of Lacy et al. (2013) and complemented by this survey. The individual fields are shown with colored arrows indicative of the minimum flux limit of each surveyed region. The area added in this paper shown by the red arrow is significantly larger than the preceding surveys, enabling the discovery of the rare luminous sources that complement the deep fields. Right: total volume surveyed vs. minimum detectable luminosity in the observed 24 μm (22 μm for the Stripe 82 area). The values are based on the survey areas and flux limits that are redshift dependent; corresponding redshifts are labeled along the curves. For illustrative purposes, we show only the SWIRE fields whose survey depths are 1 mJy (dotted line) and use their cumulative area to compute the volume. This figure demonstrates that, for a given redshift, the volume added from the Stripe 82 region is orders of magnitude larger than the other surveys and reaches sources across the redshift range.
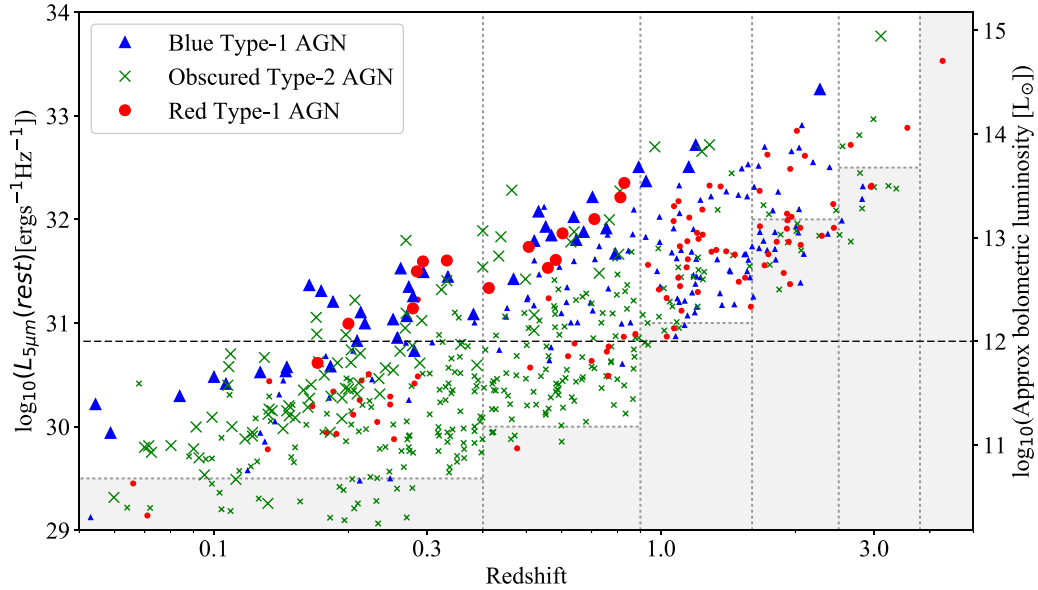
Figure 18. Luminosity vs. redshift for the objects in our survey (large symbols) plotted along with the sources in Lacy et al. (2015) (small symbols). Blue Type-1 AGNs are shown with blue triangles, obscured Type-2 AGNs are shown with green crosses, and reddened Type-1 AGNs are plotted with red circles. The dashed horizontal line marks the Seyfert/QSO divide at $\log_{10}(L_{5\mu m}) = 30.8$ erg s^{-1} Hz^{-1}. The dotted lines demarcate the redshift bins used to compute the different LFs shown in Figure 19. Objects lying in the shaded area were excluded from the binned analysis of the LF, while all objects were used in the maximum likelihood fit (this impacts only the fainter sources from Lacy et al. 2015). Note that the densities of sources seen in this figure are not representative of the relative volume densities, as they would need to be scaled by the different areas and depths sampled by each survey.

Urrutia et al. 2008; Glikman et al. 2012, 2015), which were also more common at high redshifts.

Finally, we study the fraction of AGNs that are obscured (i.e., not blue Type-1) as a function of luminosity in Figure 21. The left panel shows the total obscured fraction —combining Type-2 and red Type-1 sources—with black circles. The fraction of Type-2 sources is shown with green

circles, while the fraction of reddened Type-1 sources is plotted with red circles. The dashed lines are determined by taking a ratio of the respective fits to the different LFs. As was already seen in Lacy et al. (2015) (and previously by Treister et al. (2008) using infrared selection and Treister et al. (2009) using X-ray selection), the obscured fraction increases with decreasing luminosity and is dominated by
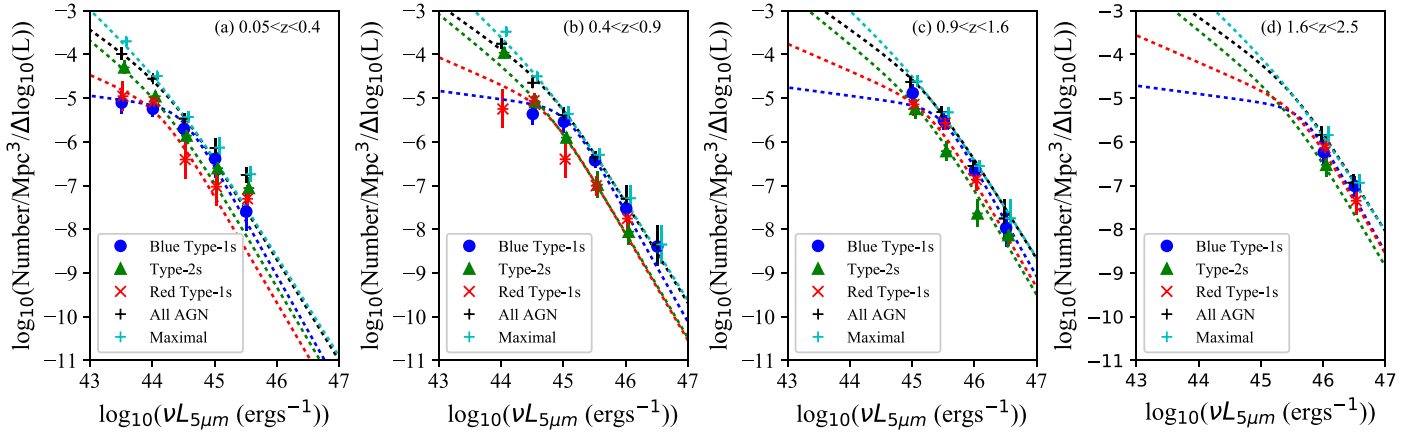
Figure 19. LF of infrared-selected AGNs for the separate AGN types considered in this paper: Type-1 (blue circles), reddened Type-1 (red crosses), and Type-2 (green triangles). The total AGN luminosity is also shown (black plus signs). Symbols represent the binned volume densities, while the dashed lines show the best-fit double power-law LF for the given redshift range determined using Equations (4) and (5).

Table 8
Best-fitting Luminosity Function Parameters

AGNs Used	n_a	$\log_{10}(\phi^* [\text{Mpc}^{-3}])$	γ_1	γ_2	k_1	k_2	k_3	$\log_{10}(L_0^* [\text{ergs}^{-1}\,\text{Hz}^{-1}])$
All	582	-4.70 ± 0.02	1.00 ± 0.06	2.31 ± 0.05	0.933 ± 0.03	-4.54 ± 0.13	-0.169 ± 0.19	31.84 ± 0.02
Normal Type-1	160	-5.23 ± 0.05	0.19 ± 0.18	2.52 ± 0.10	0.346 ± 0.08	-5.13 ± 0.23	0.286 ± 0.76	31.95 ± 0.08
Type-2	323	-5.13 ± 0.03	1.15 ± 0.12	2.41 ± 0.10	1.08 ± 0.04	-3.84 ± 0.14	-0.170 ± 0.25	31.76 ± 0.02
Red Type-1	98	-5.18 ± 0.05	0.62 ± 0.20	2.44 ± 0.12	1.14 ± 0.09	-4.93 ± 0.27	-0.047 ± 0.56	31.92 ± 0.03
Type-2+Red Type-1	421	-5.02 ± 0.03	1.11 ± 0.06	2.42 ± 0.08	1.26 ± 0.04	-3.95 ± 0.14	-0.088 ± 0.20	31.89 ± 0.01
Maximal	805	-4.67 ± 0.02	1.34 ± 0.06	2.29 ± 0.05	0.891 ± 0.03	-4.48 ± 0.13	-0.161 ± 0.19	31.82 ± 0.01

Note. n_a is the number of AGNs used in the fit. ϕ^*, γ_1, γ_2, and L_0^* are defined in Equation (4), k_1, k_2, and k_3 in Equation (5). To convert these to approximate bolometric LFs, add $\log_{10}(8.0\nu) = 14.68$ to $\log_{10}(L_0^*)$.
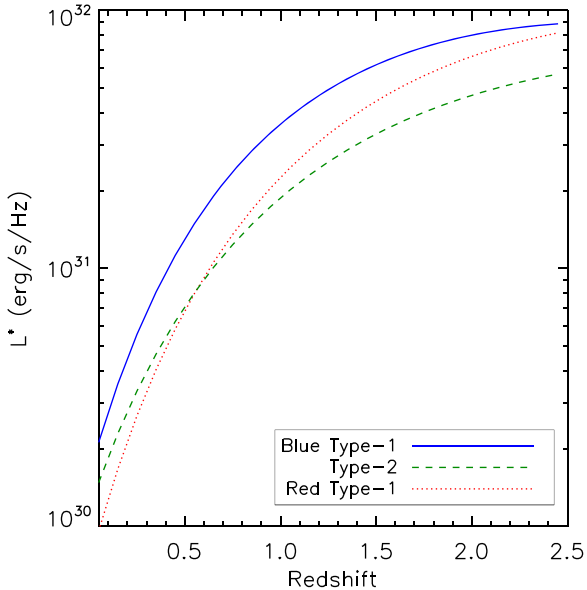
Figure 20. Evolution of L^* with redshift for the three quasar types based on our LF fits.

Type-2 sources below $\nu L_{5\mu m} \sim 10^{45}$ erg s^{-1} (corresponding to $\sim 10^{12} L_\odot$, or roughly at the Seyfert/QSO division line). It is possible that the mid-infrared color cuts imposed by our survey miss low-luminosity AGNs whose SEDs are affected by star formation. However, such sources would lack clear high-ionization emission-line signatures of AGNs in their spectra, likely due to obscuration (Eckart et al. 2010), thus amplifying the trend. At higher luminosities the fraction of Type-2 QSOs rivals that of reddened Type-1 QSOs, and at the highest luminosities reddened QSOs dominate the obscured fraction.

This analysis finds that red Type-1 QSOs make up ∼30% of the QSO population, consistent with the 27% found through the raw counting estimate in Section 5.1. However, if we consider the full luminosity range shown in Figure 21, the fraction is reduced somewhat. Both estimates are broadly consistent with luminous (above $\sim 10^{45}$ erg s^{-1}) red Type-1 QSOs making up ∼30% of the overall QSO population.

In the right panel of Figure 21 we explore the redshift dependence of the sources contributing to the fraction of obscured AGNs. For this purpose we combine Type-2 and reddened Type-1 sources and divide the sample into a low-redshift subset ($z < 0.8$; blue circles) and a high-redshift subset ($z > 0.8$; magenta circles). At low luminosities, the absence of high-redshift sources indicates our combined surveys' detection limits. The low-redshift sample is dominated by Type-2 AGNs whose density is strongly luminosity dependent; this is especially true at low luminosities, where red Type-1 quasars are rare. Thus, the luminosity dependence of the cyan points is similar to that of the green points in the left panel. However, at
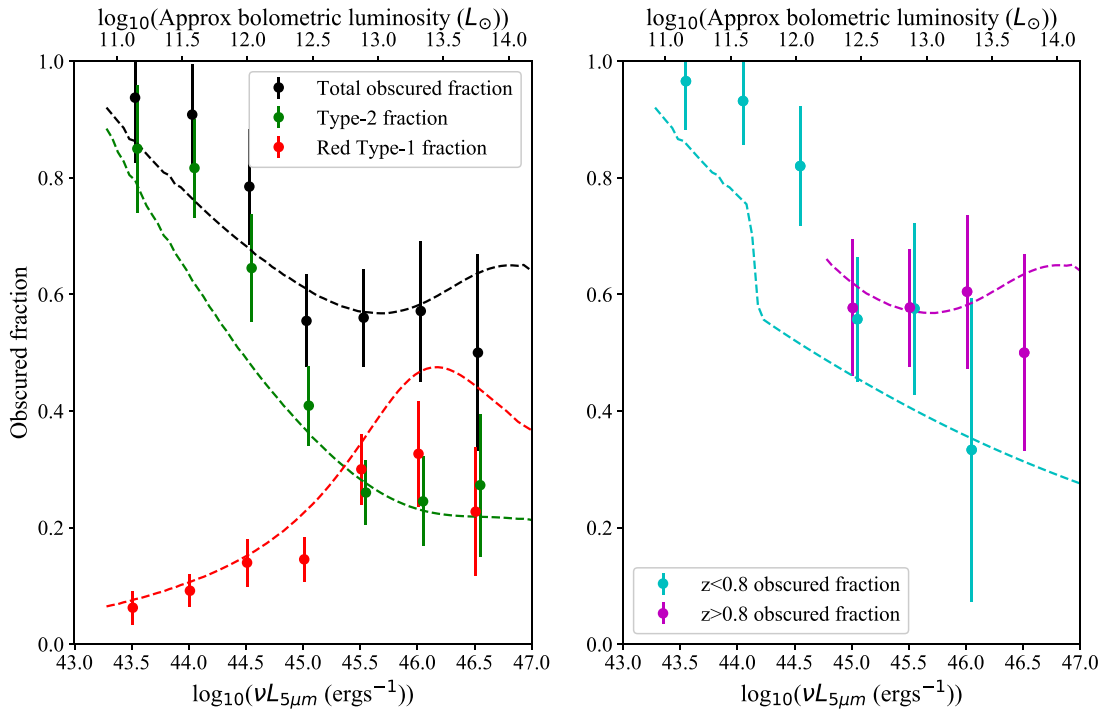
Figure 21. Fraction of AGNs that are obscured as a function of 5 μm infrared luminosity. Left: the obscured populations are broken up into Type-2 (green) and red Type-1 (red) AGNs. Evidently, red Type-1 AGNs dominate the obscured fraction at the highest luminosities, while the obscured fraction of Type-2 AGNs increases toward lower luminosities. Right: the obscured fraction is broken up into a low-redshift regime ($z < 0.8$; cyan circles) and a high-redshift regime ($z > 0.8$; magenta circles) and combines both red Type-1 and Type-2 sources. While the fraction of low-redshift obscured AGNs declines strongly with luminosity, high-redshift sources display little dependence on luminosity. This is consistent with Type-2 AGNs being a more common phenomenon at low redshift, while luminous red quasars are found in greater numbers at higher redshifts and dominate the effect seen in the magenta points.

high redshifts and high luminosities, red Type-1 AGNs begin to dominate the space density. If the red quasar phenomenon is an evolutionary phase, it may not have a strong luminosity dependence—other than being a high-luminosity phenomenon —resulting in the flat luminosity dependence seen in the magenta points (this was shown to be true for high Eddington ratio AGNs studied by Ricci et al. 2017b). In the highest-luminosity bin our survey volume is still too small to include the most luminous sources at low redshift. On the other hand, the absence of such high-luminosity sources could indicate real evolution.

6. Conclusion

We have constructed a sample of infrared-selected AGN candidates designed to be minimally sensitive to obscuration with the objective of understanding the contribution of different AGN types (Type-1, red Type-1, and Type-2) to the overall AGN population. This work focuses on the brightest sources, down to a flux limit of 20 mJy at 22 μm, in the SDSS Stripe 82 region covering $\sim$300 deg^2 to complement similar work done by Lacy et al. (2013, 2015) in deeper *Spitzer* fields covering smaller areas of sky. The sample is 100% spectroscopically complete, allowing a well-constrained study of AGN population statistics. We identified a total sample of 139 AGNs and quasars, just over half (54%) of which are blue, Type-1 AGNs. Another third (34%) are Type-2 AGNs, and the remaining eighth (12%) are reddened Type-1 AGNs.

We find the following:

1. The red quasar fraction is $\sim$30% when compared to unreddened Type-1 quasars of similar intrinsic luminosities. This is consistent with previous findings from the radio-selected F2M sample, suggesting that the red quasar fraction does not depend on their radio brightness, as was assumed in those samples, at least at the luminosities probed here.

2. A handful of these sources with detections in X-rays show that their HRs are generally consistent with expectations based on their optical and near-IR spectroscopic classifications.

3. Their X-ray luminosities correlate well with [O III] line luminosity, suggesting that both are reasonably reliable bolometric luminosity indicators. However, the most infrared-luminous AGNs appear to be relatively under-luminous in X-rays, or perhaps overluminous in IR. This trend has been noted elsewhere for similarly luminous obscured quasar populations, but is not yet understood.

4. The LFs of the three classes of AGNs have different shapes, implying that these sources have different physical origins. The space density of reddened quasars exceeds that of Type-2 quasars at the highest luminosities.

5. The LFs of the three classes of AGNs evolve differently with redshift, with reddened Type-1 AGNs dominating the infrared luminosity output at higher redshifts, while Type-2 AGNs dominate at lower redshifts.

6. The fraction of Type-2 AGNs is highest at low luminosities—below the break luminosity, L^*—at least at $z \lesssim 1$, where we are able to probe this regime. This has

been noted elsewhere (e.g., Treister et al. 2008, 2009; Assef et al. 2013; Lacy et al. 2015).

7. The fraction of reddened Type-1 AGNs increases with increasing luminosity and dominates at the highest luminosities, where our survey volume is large enough to find them. This has been noted elsewhere (Glikman et al. 2012; Banerji et al. 2015).

8. The fraction of high-luminosity, high-redshift obscured AGNs is relatively constant with luminosity. Because red Type-1 AGNs dominate this population of obscured sources, this may be due to a temporal phenomenon that is largely insensitive to AGN luminosity, such as the short-lasting "blowout" phase attributed to red quasars in previous works.

Current and upcoming wide-area X-ray surveys—including Stripe 82X, *XMM*-XXL, and *eROSITA*—will allow similar studies to be performed with X-ray-selected AGNs reaching the high-luminosity sources that are lacking at this time. This will enable a better understanding of selection effects between one wavelength regime and another, toward a complete census of supermassive black hole growth across the universe's history.

Appendix
An Interesting Object

One intriguing source that appears in our candidate sample for which we have only a near-infrared spectrum, W2M J2212 +0033, appears to lie along the line of sight toward an interacting pair of galaxies. Figure 22 shows the spectroscopic and imaging information for this system and the associated galaxy. We obtained a near-infrared spectrum for this source centered on the *WISE* coordinates, shown in the crosshairs of
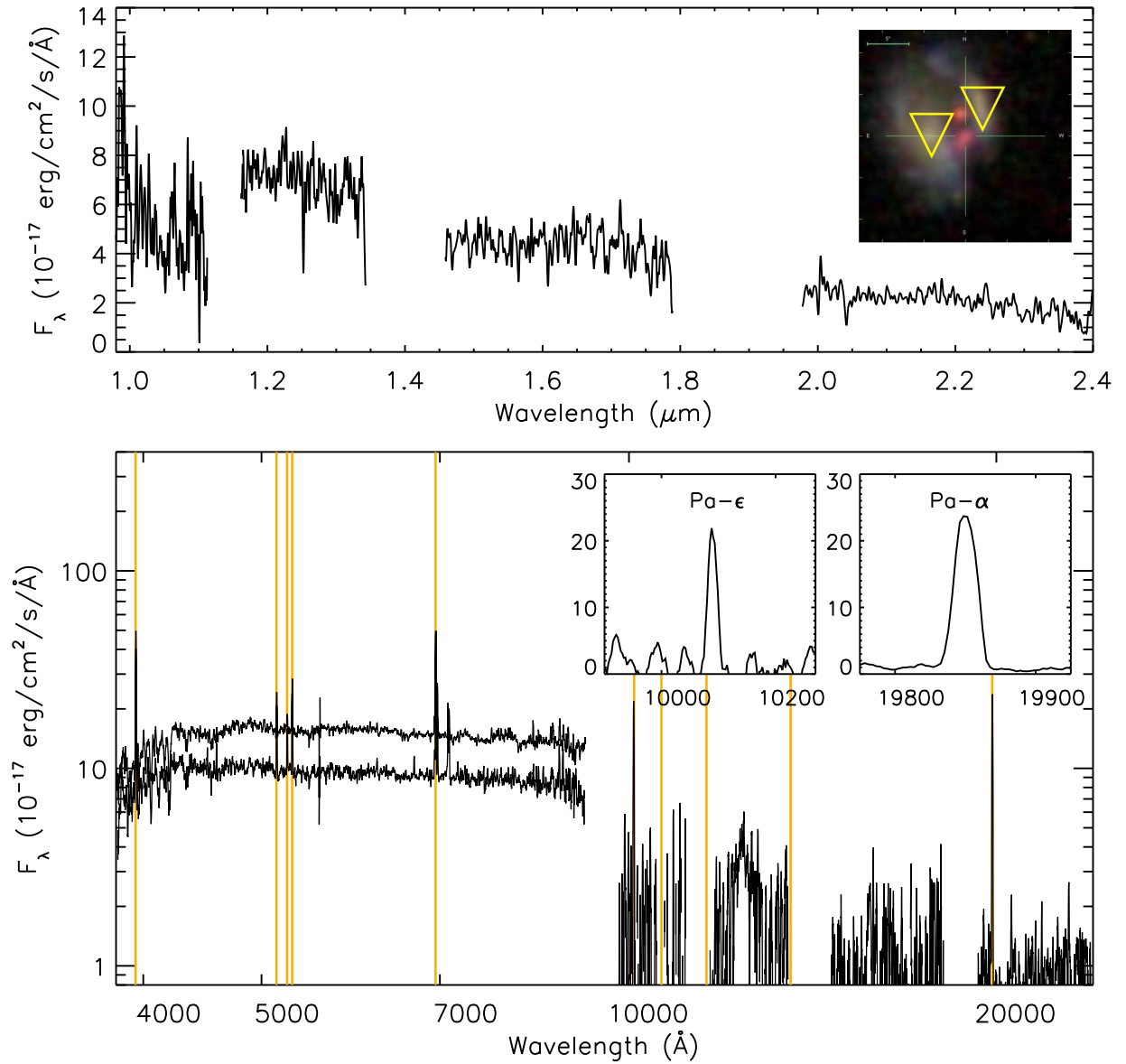
Figure 22. Spectroscopic information for the complex system W2M J2212+0033. Top panel: near-infrared spectrum of the candidate source, which appears as a red point source between two merging galaxies in the inset image. There is another bright point source to the north, which may signify a lens. However, there are no apparent lines in the near-infrared spectrum, precluding a redshift determination. Optical spectra exist for the two merging galaxy components marked with triangles in the image. Bottom panel: SDSS spectra of the left (top spectrum) and right (bottom spectrum) components of the merging galaxy. We also show, unscaled, the corresponding near-infrared emission-line spectrum, which was serendipitously detected along the slit. Prominent emission lines, [O II] $\lambda3727$, Hβ $\lambda4861$, [O III] $\lambda\lambda4959$, 5007, Hα $\lambda6563$, Paϵ $\lambda9545$, Paδ $\lambda10049$, Paγ $\lambda10941$, Paβ $\lambda12822$, and Paα $\lambda18756$, redshifted to $z = 0.058$ are marked with orange lines. The strong near-infrared emission lines Paϵ $\lambda9545$ and Paα $\lambda18756$ are shown in inset plots. Paδ $\lambda10049$ and Paγ $\lambda10941$, which lie in between, fall in regions of atmospheric absorption and are not detected.

the inset image in the top panel. The near-infrared spectrum shows no features or lines that would enable a redshift determination. The associated merging galaxies do have spectra from SDSS showing several emission lines at a redshift of $z = 0.058$. The spectra are shown in the bottom panel of Figure 22. The leftmost component in the image corresponds to the brighter spectrum, while the fainter spectrum is of the smaller arced galaxy to the right. The 2D SpeX spectrum showed extended narrow-line emission $\sim3\farcs2$ away from the target. We extracted this spectrum and identified strong, narrow Pa–ϵ and Pa–α emission, shown in the bottom panel of Figure 22 and in the inset plots. The locations of additional

Paschen lines are marked with vertical orange lines, but they fall in atmospheric absorption windows and are not detected.

ORCID iDs

E. Glikman https://orcid.org/0000-0003-0489-3750
M. Lacy https://orcid.org/0000-0002-3032-1783
S. LaMassa https://orcid.org/0000-0002-5907-3330
D. Stern https://orcid.org/0000-0003-2686-9241
S. G. Djorgovski https://orcid.org/0000-0002-0603-3087
M. J. Graham https://orcid.org/0000-0002-3168-0139
T. Urrutia https://orcid.org/0000-0001-6746-9936
M. Urry https://orcid.org/0000-0002-0745-9792

References

Ahn, C. P., Alexandroff, R., Allende Prieto, C., et al. 2012, ApJS, 203, 21

Assef, R. J., Stern, D., Kochanek, C. S., et al. 2013, ApJ, 772, 26

Baldwin, J. A., Phillips, M. M., & Terlevich, R. 1981, PASP, 93, 5

Banerji, M., Alaghband-Zadeh, S., Hewett, P. C., & McMahon, R. G. 2015, MNRAS, 447, 3368

Becker, R. H., White, R. L., Gregg, M. D., et al. 2000, ApJ, 538, 72

Becker, R. H., White, R. L., & Helfand, D. J. 1995, ApJ, 450, 559

Bennett, C. L., Larson, D., Weiland, J. L., et al. 2013, ApJS, 208, 20

Bolton, A. S., Schlegel, D. J., Aubourg, É., et al. 2012, AJ, 144, 144

Boroson, T. A., & Green, R. F. 1992, ApJS, 80, 109

Boroson, T. A., & Meyers, K. A. 1992, ApJ, 397, 442

Bruzual, G., & Charlot, S. 2003, MNRAS, 344, 1000

Chen, C.-T. J., Hickox, R. C., Goulding, A. D., et al. 2017, ApJ, 837, 145

Cushing, M. C., Vacca, W. D., & Rayner, J. T. 2004, PASP, 116, 362

Cutri, R. M., Nelson, B. O., Kirkpatrick, J. D., Huchra, J. P., & Smith, P. S. 2001, in ASP Conf. Ser. 232, The New Era of Wide Field Astronomy, ed. R. Clowes, A. Adamson, & G. Bromage (San Francisco, CA: ASP), 78

Donley, J. L., Koekemoer, A. M., Brusa, M., et al. 2012, ApJ, 748, 142

Eckart, M. E., McGreer, I. D., Stern, D., Harrison, F. A., & Helfand, D. J. 2010, ApJ, 708, 584

Elitzur, M. 2012, ApJL, 747, L33

Fan, L., Han, Y., Fang, G., et al. 2016, ApJL, 822, L32

Gallagher, S. C., Richards, G. T., Hall, P. B., et al. 2005, AJ, 129, 567

Gandhi, P., Horst, H., Smette, A., et al. 2009, A&A, 502, 457

Glikman, E., Gregg, M. D., Lacy, M., et al. 2004, ApJ, 607, 60

Glikman, E., Helfand, D. J., White, R. L., et al. 2007, ApJ, 667, 673

Glikman, E., LaMassa, S., Piconcelli, E., Urry, M., Lacy, M., et al. 2012, ApJ, 757, 51

Glikman, E., LaMassa, S., Piconcelli, E., Urry, M., & Lacy, M. 2017, ApJ, 847, 116

Glikman, E., Simmons, B., Mailly, M., et al. 2015, ApJ, 806, 218

Glikman, E., Urrutia, T., Lacy, M., et al. 2013, ApJ, 778, 127

Gregg, M. D., Lacy, M., White, R. L., et al. 2002, ApJ, 564, 133

Hall, P. B., Anderson, S. F., Strauss, M. A., et al. 2002, ApJS, 141, 267

Hamann, F., Zakamska, N. L., Ross, N., et al. 2017, MNRAS, 464, 3431

Heckman, T. M., Ptak, A., Hornschemeier, A., & Kauffmann, G. 2005, ApJ, 634, 161

Hodge, J. A., Becker, R. H., White, R. L., Richards, G. T., & Zeimann, G. R. 2011, AJ, 142, 3

Huchra, J. P., Vogeley, M. S., & Geller, M. J. 1999, ApJS, 121, 287

Ivezić, Ž., Menou, K., Knapp, G. R., et al. 2002, AJ, 124, 2364

Jia, J., Ptak, A., Heckman, T., & Zakamska, N. L. 2013, ApJ, 777, 27

Jiang, L., Fan, X., Bian, F., et al. 2014, ApJS, 213, 12

Juneau, S., Dickinson, M., Bournaud, F., et al. 2013, ApJ, 764, 176

Kauffmann, G., Heckman, T. M., Tremonti, C., et al. 2003, MNRAS, 346, 1055

Kewley, L. J., Dopita, M. A., Sutherland, R. S., Heisler, C. A., & Trevena, J. 2001, ApJ, 556, 121

Kewley, L. J., Groves, B., Kauffmann, G., & Heckman, T. 2006, MNRAS, 372, 961

Kim, D., Im, M., Glikman, E., Woo, J.-H., & Urrutia, T. 2015, ApJ, 812, 66

Kinney, A. L., Calzetti, D., Bohlin, R. C., et al. 1996, ApJ, 467, 38

Lacy, M., Petric, A. O., Sajina, A., et al. 2007, AJ, 133, 186

Lacy, M., Ridgway, S. E., Gates, E. L., et al. 2013, ApJS, 208, 24

Lacy, M., Ridgway, S. E., Sajina, A., et al. 2015, ApJ, 802, 102

Lacy, M., Storrie-Lombardi, L. J., Sajina, A., et al. 2004, ApJS, 154, 166

LaMassa, S. M., Civano, F., Brusa, M., et al. 2016a, ApJ, 818, 88

LaMassa, S. M., Heckman, T. M., Ptak, A., et al. 2009, ApJ, 705, 568

LaMassa, S. M., Heckman, T. M., Ptak, A., et al. 2010, ApJ, 720, 786

LaMassa, S. M., Heckman, T. M., Ptak, A., et al. 2011, ApJ, 729, 52

LaMassa, S. M., Ricarte, A., Glikman, E., et al. 2016b, ApJ, 820, 70

LaMassa, S. M., Urry, C. M., Cappelluti, N., et al. 2013a, MNRAS, 436, 3581

LaMassa, S. M., Urry, C. M., Cappelluti, N., et al. 2016c, ApJ, 817, 172

LaMassa, S. M., Urry, C. M., Glikman, E., et al. 2013b, MNRAS, 432, 1351

Lawrence, A., Warren, S. J., Almaini, O., et al. 2007, MNRAS, 379, 1599

Lutz, D., Maiolino, R., Spoon, H. W. W., & Moorwood, A. F. M. 2004, A&A, 418, 465

Massey, P., & Gronwall, C. 1990, ApJ, 358, 344

Mateos, S., Alonso-Herrero, A., Carrera, F. J., et al. 2012, MNRAS, 426, 3271

Mendez, A. J., Coil, A. L., Aird, J., et al. 2013, ApJ, 770, 40

Messias, H., Afonso, J. M., Salvato, M., Mobasher, B., & Hopkins, A. M. 2014, A&A, 562, A144

Oke, J. B., Cohen, J. G., Carr, M., et al. 1995, PASP, 107, 375

Panessa, F., Bassani, L., Cappi, M., et al. 2006, A&A, 455, 173

Papovich, C., Shipley, H. V., Mehrtens, N., et al. 2016, ApJS, 224, 28

Park, T., Kashyap, V. L., Siemiginowska, A., et al. 2006, ApJ, 652, 610

Rayner, J. T., Toomey, D. W., Onaka, P. M., et al. 2003, PASP, 115, 362

Ricci, C., Assef, R. J., Stern, D., et al. 2017a, ApJ, 835, 105

Ricci, C., Trakhtenbrot, B., Koss, M. J., et al. 2017b, Natur, 549, 488

Richards, G. T., Hall, P. B., Vanden Berk, D. E., et al. 2003, AJ, 126, 1131

Richards, G. T., Strauss, M. A., Fan, X., et al. 2006, AJ, 131, 2766

Ross, N. P., Hamann, F., Zakamska, N. L., et al. 2015, MNRAS, 453, 3932

Sarzi, M., Falcón-Barroso, J., Davies, R. L., et al. 2006, MNRAS, 366, 1151

Schaerer, D., Contini, T., & Pindao, M. 1999, A&AS, 136, 35

Schmitt, H. R., Donley, J. L., Antonucci, R. R. J., Hutchings, J. B., & Kinney, A. L. 2003, ApJS, 148, 327

Skrutskie, M. F., Cutri, R. M., Stiening, R., et al. 2006, AJ, 131, 1163

Stanford, S. A., Stern, D., van Breugel, W., & De Breuck, C. 2000, ApJS, 131, 185

Stern, D. 2015, ApJ, 807, 129

Stern, D., Assef, R. J., Benford, D. J., et al. 2012, ApJ, 753, 30

Stern, D., Eisenhardt, P., Gorjian, V., et al. 2005, ApJ, 631, 163

Storchi-Bergmann, T., Kinney, A. L., & Challis, P. 1995, ApJS, 98, 103

Strauss, M. A., Huchra, J. P., Davis, M., et al. 1992, ApJS, 83, 29

Taylor, M. B. 2005, in ASP Conf. Ser. 347, Astronomical Data Analysis Software and Systems XIV, ed. P. Shopbell, M. Britton, & R. Ebert (San Francisco, CA: ASP), 29

Timlin, J. D., Ross, N. P., Richards, G. T., et al. 2016, ApJS, 225, 1

Treister, E., Krolik, J. H., & Dullemond, C. 2008, ApJ, 679, 140

Treister, E., & Urry, C. M. 2005, ApJ, 630, 115

Treister, E., Urry, C. M., Van Duyne, J., et al. 2006, ApJ, 640, 603

Treister, E., Virani, S., Gawiser, E., et al. 2009, ApJ, 693, 1713

Trouille, L., Barger, A. J., & Tremonti, C. 2011, ApJ, 742, 46

Tsai, A.-L., & Hwang, C.-Y. 2017, ApJ, 842, 57

Tsai, C.-W., Eisenhardt, P. R. M., Wu, J., et al. 2015, ApJ, 805, 90

Ueda, Y., Hashimoto, Y., Ichikawa, K., et al. 2015, ApJ, 815, 1

Urrutia, T., Becker, R. H., White, R. L., et al. 2009, ApJ, 698, 1095

Urrutia, T., Lacy, M., & Becker, R. H. 2008, ApJ, 674, 80

Urrutia, T., Lacy, M., Spoon, H., et al. 2012, ApJ, 757, 125

Urry, C. M., & Padovani, P. 1995, PASP, 107, 803

Vacca, W. D., Cushing, M. C., & Rayner, J. T. 2003, PASP, 115, 389

Veilleux, S., & Osterbrock, D. E. 1987, ApJS, 63, 295

Veilleux, S., Rupke, D. S. N., Kim, D.-C., et al. 2009, ApJS, 182, 628

Webster, R. L., Francis, P. J., Peterson, B. A., Drinkwater, M. J., & Masci, F. J. 1995, Natur, 375, 469

White, R. L., Helfand, D. J., Becker, R. H., et al. 2003, AJ, 126, 706

Wilson, J. C., Henderson, C. P., Herter, T. L., et al. 2004, Proc. SPIE, 5492, 1295

Wright, E. L. 2006, PASP, 118, 1711

Wright, E. L., Eisenhardt, P. R. M., Mainzer, A. K., et al. 2010, AJ, 140, 1868

Wu, J., Jun, H. D., Assef, R. J., et al. 2018, ApJ, 852, 96

Wu, J., Tsai, C.-W., Sayers, J., et al. 2012, ApJ, 756, 96

York, D. G., Adelman, J., Anderson, J. E., Jr., et al. 2000, AJ, 120, 1579